Spring 2015

Optimizing electrode thickness and material for laser-induced electrothermal flow

Jian Wei Khor
Purdue University

Graduate School Form 30
Updated 1/15/2015

PURDUE UNIVERSITY
GRADUATE SCHOOL
Thesis/Dissertation Acceptance

This is to certify that the thesis/dissertation prepared

By Jian-Wei Khor

Entitled

OPTIMIZING ELECTRODE THICKNESS AND MATERIAL FOR LASER-INDUCED ELECTROTHERMAL FLOW

For the degree of Master of Science in Mechanical Engineering

Is approved by the final examining committee:

Steven T. Wereley
Chair

Jun Chen

Liang Pan

To the best of my knowledge and as understood by the student in the Thesis/Dissertation Agreement, Publication Delay, and Certification Disclaimer (Graduate School Form 32), this thesis/dissertation adheres to the provisions of Purdue University's "Policy of Integrity in Research" and the use of copyright material.

Approved by Major Professor(s): Steven T. Wereley

Approved by: Ganesh Subbarayan 4/15/2015

Head of the Departmental Graduate Program Date

OPTIMIZING ELECTRODE THICKNESS AND MATERIAL FOR LASER-INDUCED ELECTROTHERMAL FLOW

A Thesis

Submitted to the Faculty

of

Purdue University

by

Jian-Wei Khor

In Partial Fulfillment of the

Requirements for the Degree

of

Master of Science in Mechanical Engineering

May 2015

Purdue University

West Lafayette, Indiana

ACKNOWLEDGMENTS

First and foremost, I would like to thank my parents for supporting me financially and emotionally throughout my graduate studies at Purdue University. They have provided me with ease of mind, which contributed to my total focus in my studies and research. I would also like to thank my fiancé, Ling Sim Hong, for encouraging me to pursue my goals and had faith in my endeavors.

I would also like to thank Professor Steven Wereley who is my academic advisor for guiding me through my graduate research. He has inspired me to do good research and made me understand the workings of academia. I am also grateful for being able to use the overpriced equipments in his research lab.

I would like to thank my lab mates, Avanish Mishra, Katie Clayton, Raviraj Thakur, and Nathan Miller, lab alumni, Dr. Stuart Williams, Dr. Craig Snoeyink, and Dr. Jaesung Kwon, and previous visiting scholars, Dr. Xudong Pan and Comlan Magloire, for giving me advice and guidance on the proper procedures to conduct research. I would like to specifically acknowledgement Avanish Mishra as he has been my mentor for all of my undergraduate and graduate research.

Avanish has followed my research very closely and has trained me to become a better researcher.

TABLE OF CONTENTS

Page
LIST OF TABLES ……v
LIST OF FIGURES……vi
ABSTRACT……ix
CHAPTER 1: BRIEF INTRODUCTION OF MICROFLUIDICS ……1
CHAPTER 2: RAPID ELECTROKINETIC PATTERNING……3
2.1 Introduction ……3
2.2 Physics……5
2.2.1 Electrothermal Flow……6
2.2.2 Particle-Electrode Interaction……8
2.2.3 Dielectrophoresis……10
2.2.4 Particle Dipole-Dipole Attraction……16
2.2.5 Parameters for Particle Clustering ……24
2.3 Methodology……27
2.4 Current Applications……30
2.4.1 Differentiation of Biological Organisms……30
2.4.2 Plasmonic Nanostructure to Optimize REP……32
2.4.3 REP in Coplanar Electrodes ……33
2.4.4 Thin Film Heaters as Heat Source for REP……34
2.5 Conclusions and Future Work……35
CHAPTER 3: OPTIMIZING ELECTRODE THICKNESS AND MATERIAL FOR LASER-INDUCED ELECTROTHERMAL FLOW……36
3.1 Introduction……36
3.2 Theory……38
3.2.1 Reflection of the Laser at the Electrode Surface……38
3.2.2 Production of Temperature Gradient in Electrodes……39
3.2.3 Analytical Solution of Laser Heating onto a Thin Substrate……40
3.2.4 AC Electric Field in Solution……41
3.2.5 Fluid Mechanics and Electrothermal Flow ……41
3.3 Method and Materials……42
3.3.1 Chip Design and Fabrication……42
3.3.2 Experimental Setup……43
3.3.3 Particle Preparation……44
3.3.4 Software and Image Processing……44
3.4 Numerical Simulations……45
3.4.1 Production of Temperature Gradient in Electrodes……46
3.4.2 AC Electric Field in Solution……47

Page

3.4.3 Electrothermal Flow……47
3.4.4 Simulation……48
3.4.5 Comparison Between Experimental Results and Computational Results……53
3.5 Results and Discussions……54
3.5.1 Analytical Results of Temperature Difference per Laser Power ……55
3.5.2 Analytical Solution and Computational Results of the Temperature Gradient……57
3.5.3 Comparison of Flow Velocity of Electrothermal Flow for Materials of Similar Thickness……60
3.5.4 Optimal Material Thickness for Electrothermal Flow……62
3.6 Conclusion……63
LIST OF REFERENCES……65
VITA……68

LIST OF TABLES

Table Page
Table 1: Values of important properties for numerical simulation……..49
Table 2: Properties of various materials……..54

LIST OF FIGURES

Figure Page
Figure 1: Rapid Electrokinetic Patterning (REP). (a) Velocity profile of electrothermal flow. (b) A 3D trajectory of the electrothermal flow at 200 kHz. (Fig. 1b printed with permission from Kumar et al. Copyright 2010 Springer) [5]. (c-e) Particles being trapped into a cluster using REP.....4
Figure 2: Physics of Rapid Electrokinetic Patterning. (a) Force relationship on a particle during REP. (b-c) The clustering of particles when laser is turned on. (d) The temperature increse on an ITO coverslip and (e) the effect of different laser powers and the temperature profile produced. (Fig. 2d and 2e reprinted with permission from Kumar et al. Copyright 2010 American Chemical Society) [6].....6
Figure 3: Polarization of Particles. (b) shows a neutral particle when there is no applied electric field and (c) shows a polarized particle due to an electric field.....8
Figure 4: Electric Double Layer.....9
Figure 5: Positive and negative dielectrophoresis for more polarizable particle and less polarizable particle in uniform (a) and non-uniform electric field (b). 13
Figure 6: Plot of the Clausius-Mossotti factor for two different particles (solid and dotted lines) with respect to Frequency and the Separation of Particles using Dielectrophoresis.....15
Figure 7: Dipole Moment. 16
Figure 8: Attraction of two Fixed Dipoles.....17
Figure 9: Particle-particle Interaction where two particles are aligned parallel to the electric field. (a) has particles that are more conductive than the solution and (b) has particles that are less conductive than the solution.....18
Figure 10: Particle-particle Interaction where two particles that are aligned perpendicular to the electric field.....19
Figure 11: Particle-particle Interaction where two different particles are aligned parallel (a) and perpendicular (b) to the electric field.....21
Figure 12: Chain forming of different particles in a solution applied with an electric field.....23

Figure Page

Figure 13: Accumulation of 1.0 um particles at the ITO electrode over a period of 3 min for various peak-to-peak voltages. Laser power is 23 mW and AC frequency is 70 kHz. (© IOP Publishing. Reproduced from Williams et al. by permission of IOP Publishing) [7]……24
Figure 14: Accumulation of 1.0 um particles at the ITO electrode over a period of 3 min for various frequencies. Laser power is 23 mW and AC peak-to-peak voltage is 15.3 V_{pp}. (© IOP Publishing. Reproduced from Williams et al. by permission of IOP Publishing) [7]……25
Figure 15: Accumulation of 1.0 um particles at the ITO electrode over a period of 3 min for various frequencies. AC peak-to-peak voltage is 15.3 V_{pp}. and AC frequencty is 70 kHz. (© IOP Publishing. Reproduced from Williams et al. by permission of IOP Publishing) [7]……26
Figure 16: Maximum trapping frequency for particles of various diameters to cluster at different applied AC peak-to-peak voltage. Laser power is 23 mW. [7]……27
Figure 17: REP Chip……28
Figure 18: REP Setup……29
Figure 19: Trapping and Translation of S. oneidensis. (Reprinted with permission from Kwon et al. Copyright 2012 Royal Society of Chemistry)[18]……30
Figure 20: Separation of S. aureus from S. cerevisae. (Reprinted with permission from Kwon et al. Copyright 2012 Royal Society of Chemistry)[18]……31
Figure 21: Plasmonic nanostructures: The velocity distribution (a) and radial velocity (b). (Reprinted with permission from Ndukaife et al. Copyright 2014 American Chemical Society)[19]……32
Figure 22: Twin Opposing Microvortices (TOMV). (Reprinted with permission from Park et al. Copyright 2012 Royal Society of Chemistry)[20]……33
Figure 23: Conducting REP using thin film heaters as heat source (Reprinted with permission from Velasco et al. Copyright 2012 Elsevier) [21 & 22]……34
Figure 24: Illustration of REP with laser focused at the top electrode……36
Figure 25: Propagation of Light (Reflection and Refraction) in Materials……38
Figure 26: Experimental Setup and Method……45
Figure 27: (a) Boundary conditions of the geometry in the simulation. E: AC Electric Field Model. H: Heat Transfer Model. F: Computational Fluid Dynamics Model. (b) Vector field of simulated electrothermal flow in logarithmic scale. (c) Contour plot of simulated electrothermal flow……48
Figure 28: Final Geometry……50
Figure 29: Free triangular meshing (top and bottom) and quadrilateral meshing (center)……52

Figure Page

Figure 30: Comparison of velocity profiles of electrothermal flow of 40 nm Ti from experimental results and simulation at the same location. ……..54
Figure 31: Temperature rise per laser power of Ni at (a) and Ti at (b) from analytical results……..55
Figure 32: Temperature gradient of Ni at (a) and Ti at (b) from analytical results……..57
Figure 33: Steepest temperature gradient for ITO, Ni and Ti from analytical results……58
Figure 34: Temperature gradient of Ni at (a) and Ti at (b) from computational results……..59
Figure 35: Steepest temperature gradient for ITO, Ni and Ti from computation results……60
Figure 36: Experimental velocity profile of electrothermal flow by ITO, Ni and Ti of similar thicknesses at 30 V peak to peak and 201.8 μm above the bottom substrate in the channel……60
Figure 37: The relationship of the maximum velocity produced in the corresponding thickness for ITO at (a) and Ni and Ti at (b) at 30 V peak to peak and at 201.8 μm above the bottom substrate in the channel……62

ABSTRACT

Khor, Jian-Wei, M.S.M.E., Purdue University, May 2015. Optimizing Electrode Thickness and Material for Laser-Induced Electrothermal Flow. Major Professor: Steven T. Wereley, School of Mechanical Engineering

In this article, the material dependence of electrothermal flow is studied to optimize an optoelectric particle manipulation technique called Rapid Electrokinetic Patterning (REP). REP utilizes a heat source to produce temperature gradients, which, in this study, are induced by the application of a 1064 nm cw laser. The simultaneous application of an uniform AC electric field assemble colloids on the surface of an electrode that can be moved by translating the laser. The temperature gradients produced from the heat source are crucial in REP as the higher the temperature gradient the faster the electrothermal flow. Thus, optimization of temperature gradients would enhance REP performance with lower laser power. In this study, material properties of the electrode that produces the temperature gradient in REP are investigated to understand the absorption of the radiation from the laser. Analytical, computational and experimental aspects of the phenomenon were studied. It was found that the analytical model and the computation model could be used to select the optimum material and thickness of the electrode to

produce the highest temperature gradient per watt of laser power. Furthermore, the computational model can be used to determine the flow velocity of the electrothermal flow accurately. With this study material selection of the electrode can be calibrated and customized for specific needs when conducting REP. It was found that among the materials tested (ITO, titanium, and nickel), the best material that produced the highest temperature gradient was titanium followed by nickel and ITO. When comparing the three materials with approximately the same thicknesses, it was observed that the maximum velocity magnitude produced by titanium and nickel electrodes were almost 80 times higher than the ITO electrodes.

CHAPTER 1: BRIEF INTRODUCTION OF MICROFLUIDICS

Microfluidics has been an emerging field in the past two decades and there is still potential for it to become more prominent in the future as scientists and engineers come up with new applications for microfluidics. The research interests toward microfluidics mostly stem from the fact that the study of microfluidics, which is the study of fluid mechanics in the micro-scale, can open up many opportunities in the fields of biomedical science and chemistry [1, 2]. Due to the fact that it is microscale, flows in microfluidics are mostly Stokes flow (flow of low Reynold's number), which is relatively easy to study physically compared to high Reynold's flow and also easy to manipulate.

Being able to control micro-scale fluid has many benefits. Firstly, tasks that are not dependent on volume can be miniaturized. For example, chemical analyses that are common in drug diagnostics, biological analysis, and etc. do not depend on the volume of the sample but rather ratios of sample volume to reagents to produce results. By being able to control micro-scale fluid, the samples can be reduced by 1000 times or more. Consequently, microfluidics can also prevent wastage. Apart from being able to reduce the volume of the sample, analyses can be calibrated so that there won't be any excess of samples and reagents when conducting the analysis.

Thus, microfluidics could be a good tool for many biomedical and chemical applications as it reduces sample and reagent size and reduce wastage.

In recent years, a new optoelectric method named Rapid Electrokinetic Patterning (REP) had been developed by Williams et al [3-9]. REP is a particle manipulation technique that is used to differentiate and aggregate particles into clusters from a mixture of particles of different sizes. Furthermore, REP also can translate particle clusters from one location to another. This technique could possibly be used in many applications like biosensing, nanostructure fabrication and etc.

CHAPTER 2: RAPID ELECTROKINETIC PATTERNING

2.1 Introduction

In recent years, innovations in microfluidics like Lab-on-a-Chip (LOC) have been an emergent technology that could have an impact in biomedical application [1, 2]. Simple tasks like manipulating, separating, sorting, and mixing are highly desirable in the biomedical community as these tasks would allow them to be able to conduct laboratory analysis with only a small amount of samples and be able to conduct it on a platform that could be the size of a credit card [1, 2].

REP is an electrokinetic method that can simultaneously accumulate a cluster of particles of a specific size and manipulate the cluster [3-9]. It requires a heat source like a laser or heaters to provide a temperature gradient and also an AC electrical power source to provide an electric field gradient. There are many benefits to conducting REP. First of all, REP is a non-contact high-speed manipulation method where one can accumulate a cluster of particles in the matter of seconds. Furthermore, REP is a very consistent technique where clusters will consistently form when conducting it. Also, REP chips are very simple to produce and can be fabricated in any laboratory that has the right materials.

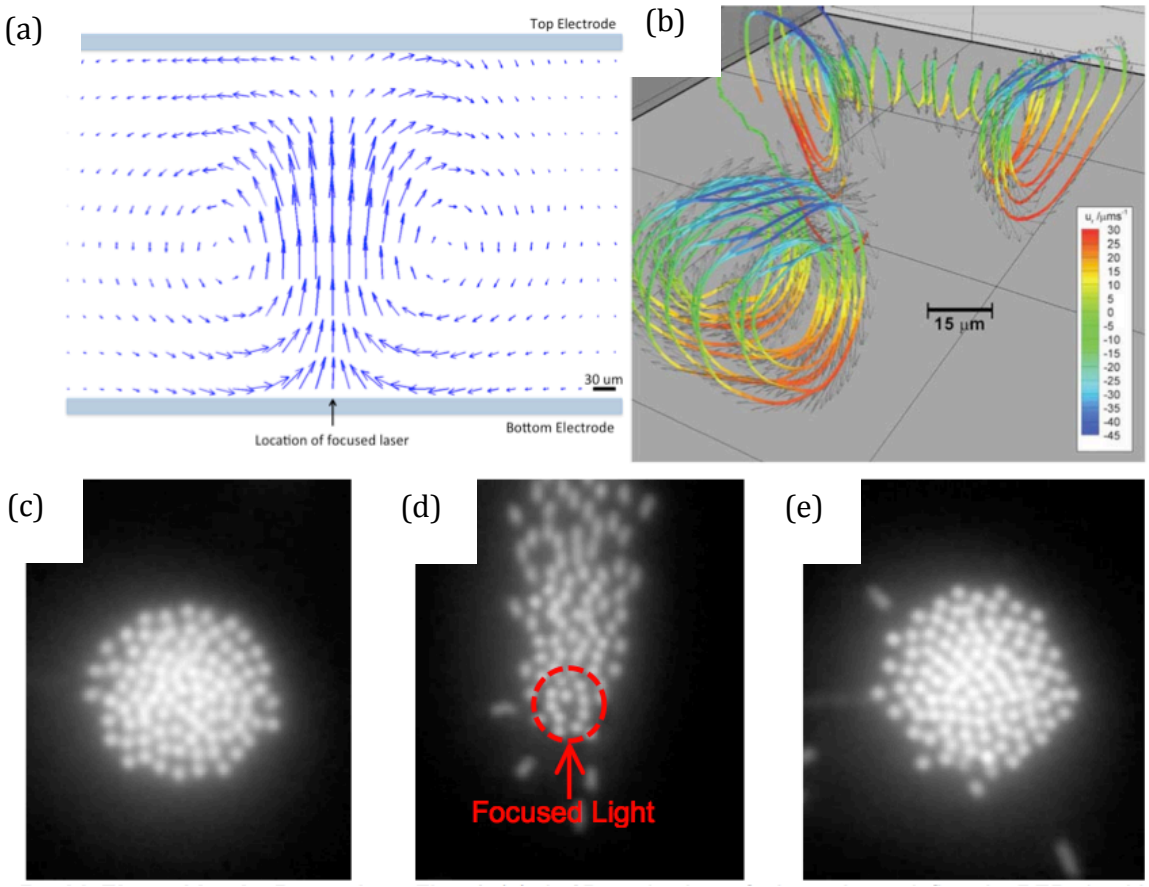

Figure 1: Rapid Electrokinetic Patterning (REP). (a) Velocity profile of electrothermal flow. (b) A 3D trajectory of the electrothermal flow at 200 kHz. (Fig. 1b printed with permission from Kumar et al. Copyright 2010 Springer) [5]. (c-e) Particles being trapped into a cluster using REP.

On the other hand, REP also has its limitations. REP is only conducted in a small area that is of micrometer length scales. Large-scale conduction of REP will require higher power and a more complex setup. Furthermore, the temperature gradient or electric field gradient needed to conduct REP could be too unbearable for the samples and could permanently alter the samples structure [10]. However, by having this in mind, power needed to conduct REP can be calibrated and reduced to eliminate damage to these samples. As of now, there has been no finding that

suggest REP can potentially damage a kind of sample and further studies are being extended to investigate the potential damage of REP that could be applied onto the samples.

2.2 Physics

REP consists of three major components: electrothermal flow, particle-particle interaction, and particle-electrode interaction. Currently, particle-particle interaction and particle-electrode interaction in REP has not been well studied and studies are being done to understand these phenomenon. On the other hand, electrothermal flow has been very well studied and its theoretical foundation is well established [11-16].

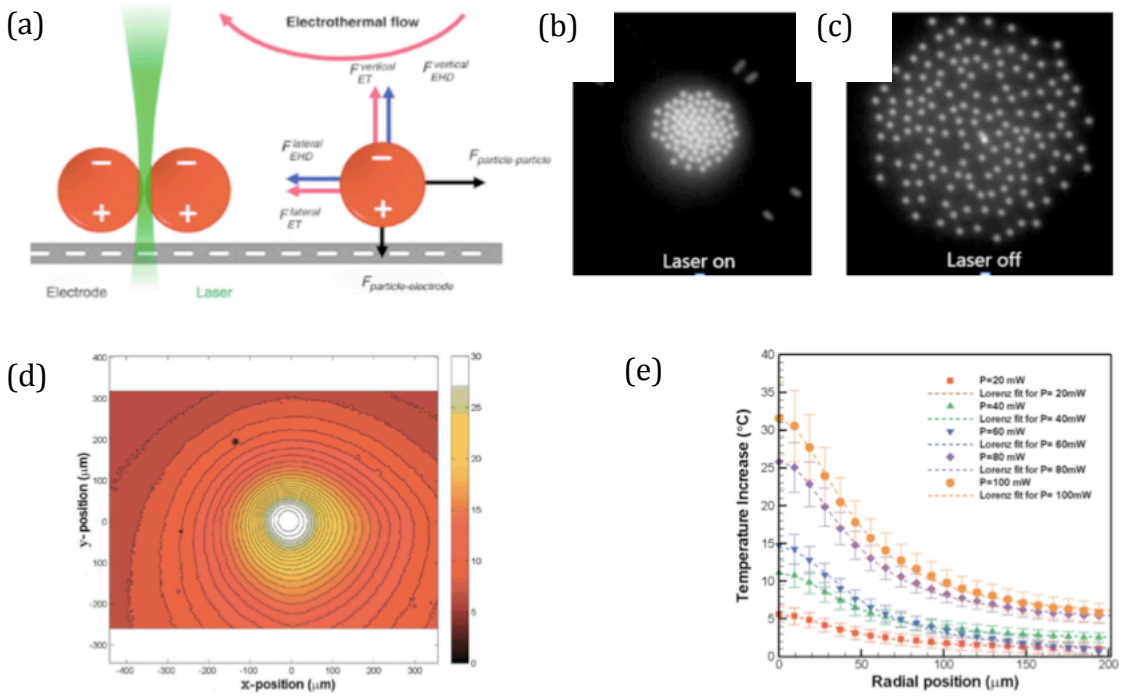

Figure 2: Physics of Rapid Electrokinetic Patterning. (a) Force relationship on a particle during REP. (b-c) The clustering of particles when laser is turned on. (d) The temperature increse on an ITO coverslip and (e) the effect of different laser powers and the temperature profile produced. (Fig. 2d and 2e reprinted with permission from Kumar et al. Copyright 2010 American Chemical Society) [6].

2.2.1 Electrothermal Flow

Electrothermal flow is a flow that is produced from an AC electric field and a temperature gradient [11-16]. Temperature gradient causes conductivity and permittivity gradients in the fluid which causes microvortices to form due to actuation by an AC electric field on the fluid. Electrothermal flow is used in REP to concentrate particles onto the laser spot to increase the instances of particle-particle interaction.

Equation (1) describes the time averaged electrothermal body force [11-16].

$$\left\langle f_{ET} \right\rangle = \frac{\varepsilon_m}{2}\left(\left(\frac{1}{\varepsilon_m}\frac{\partial \varepsilon_m}{\partial T} - \frac{1}{\sigma_m}\frac{\partial \sigma_m}{\partial T}\right)\frac{\nabla T \bullet E}{1+\left(\omega \frac{\varepsilon_m}{\sigma_m}\right)^2} E - \frac{1}{2}\frac{1}{\varepsilon_m}\frac{\partial \varepsilon_m}{\partial T}\left|E\right|^2 \nabla T\right) \quad (1)$$

where ε_s is the permittivity of the solution, E is the applied AC electric field derived from Equation (1), ω is the angular frequency of the AC electric field. The electrothermal body force has two force components. The Coulomb force is the component on the left and the dielectric force is the component on the right.

2.2.2 Particle-Electrode Interaction

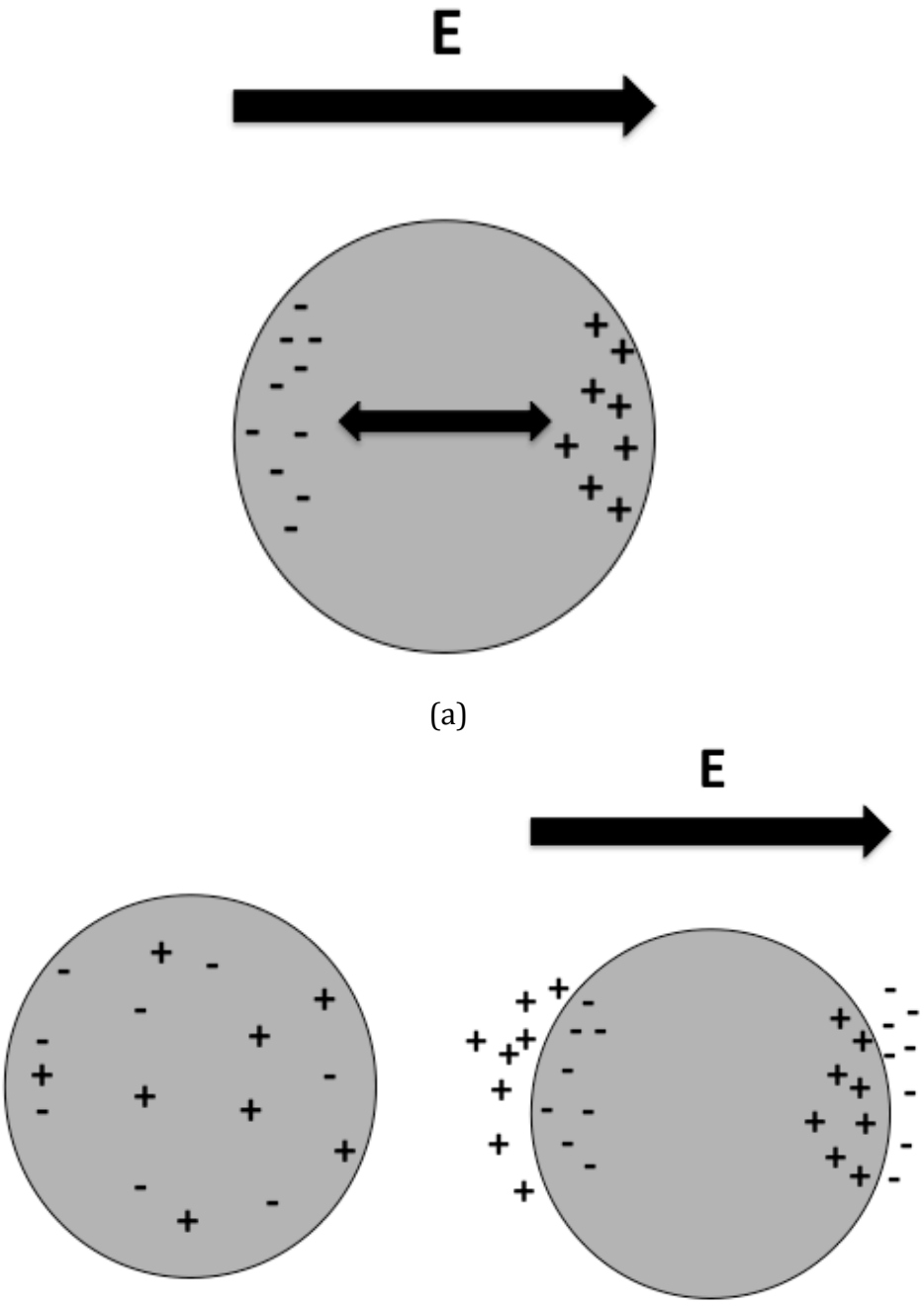

(a)

(b) (c)

Figure 3: Polarization of Particles. (b) shows a neutral particle when there is no applied electric field and (c) shows a polarized particle due to an electric field.

A neutral particle in an electric field becomes polarized due to the electric field. This is called an induced dipole. Dipoles will be discussed in Section 2.2.4. The positive charges would want to migrate to the part of the particle which is parallel to the direction of the electric field while the negative charges would want to migrate to the part of the particle which is opposite of the electric field. Furthermore, by following the same reasoning, the polarized particle would also attract opposite charged ions to its corresponding surface forming a layer. This layer is called the electrical double layer. [17]

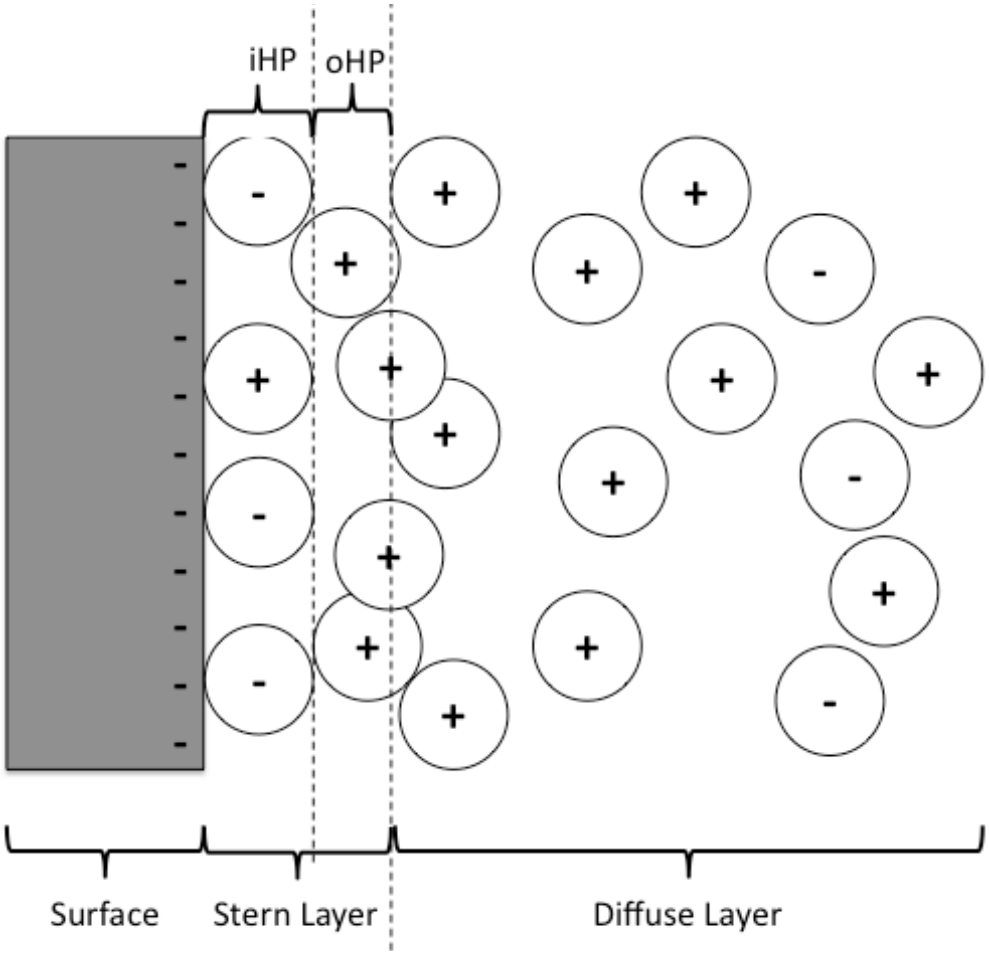

Figure 4: Electric Double Layer.

The electric double layer can be divided into three layers, the inner Helmholtz layer (iHP), the outer Helmholtz layer (oHP) and the diffuse layer. The diffuse layer is a region where the concentration of charged ions opposite to the charge of the surface charge is higher than the bulk solution. The combined inner and outer Helmholtz layers are called the Stern layer. The inner Helmholtz layer consists of non-hydrated ions that have specifically adsorbed to the surface and the outer Helmholtz layer consists of a layer of bound hydrated ions (hydration not shown in Figure 4). Looking at Figure 4 as an example, the inner Helmholtz layer can consist of both positive and negative ions while the outer Helmholtz layer consists of only positive ions. This is true for a positive surface charge as well with the exception that positive ions are replaced by negative ions and vice versa. [17]

2.2.3 Dielectrophoresis

The polarizability of a particle is governed by the permittivity and conductivity of the particle and the solution. Thus, the permittivity and conductivity of the particle and the solution has a property called the complex permittivity [17]. The complex permittivity is

$$\varepsilon = \varepsilon_0 \varepsilon_r - i\frac{\sigma}{\omega} \tag{2}$$

where ε_0 is the permittivity of free space, ε_r is the relative permittivity, i is the imaginary number, σ is the electrical conductivity, ω is the angular frequency of the AC electric field.

The magnitude of the polarizability is frequency dependent. This dependence is described by the Clausius-Mossotti factor particle (p) and solution (s) [17]

$$f_{CM}(\varepsilon_p, \varepsilon_s) = \frac{\varepsilon_p - \varepsilon_s}{\varepsilon_p + 2\varepsilon_s} \tag{3}$$

This decribes the relaxation in the polarizability of the particle with a relaxation time of [17]

$$\tau_{MW} = \frac{\varepsilon_p + 2\varepsilon_s}{\sigma_p + 2\sigma_s} \tag{4}$$

The inverse of the relaxation time is often referred to the Maxwell-Wagner relaxation frequency [17].

Dielectrophoresis is the force induced on polarized particles in an electric field. Furthermore, the force on a dipole in an electric field is [17]

$$F = (p \bullet \nabla) E \tag{5}$$

Where E is the electric field.

Thus, the time-averaged dielectrophoretic force is [17]

$$\left\langle F_{DEP} \right\rangle = \pi \varepsilon_s a^3 \, \mathrm{Re}\left[\frac{\varepsilon_p - \varepsilon_s}{\varepsilon_p + 2\varepsilon_s} \right] \nabla \left| E \right|^2 \tag{6}$$

Where ε is the permittivity, a is the radius of the particle, subscript p denotes the particle while subscript s the solution, and E is the electric field.

It is important to understand that, apart from the electric field, the Clausius-Mossotti factor is the other parameter that determines the direction of the dielectrophoretic force on the particle. A positive value in the Clausius-Mossotti factor will cause a positive dielectrophoretic force while a negative value in the Clausius-Mossotti factor will cause a negative dielectrophoretic force.

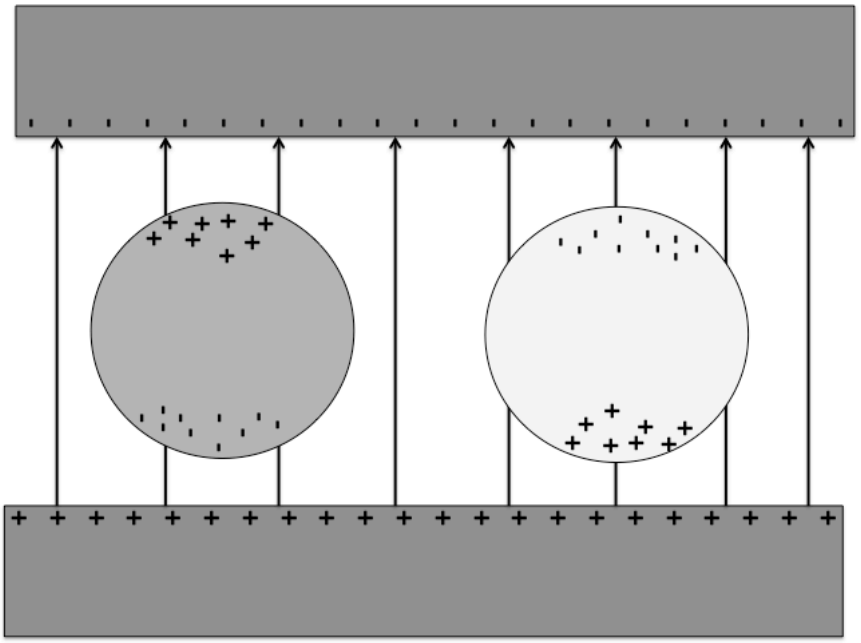

(a)

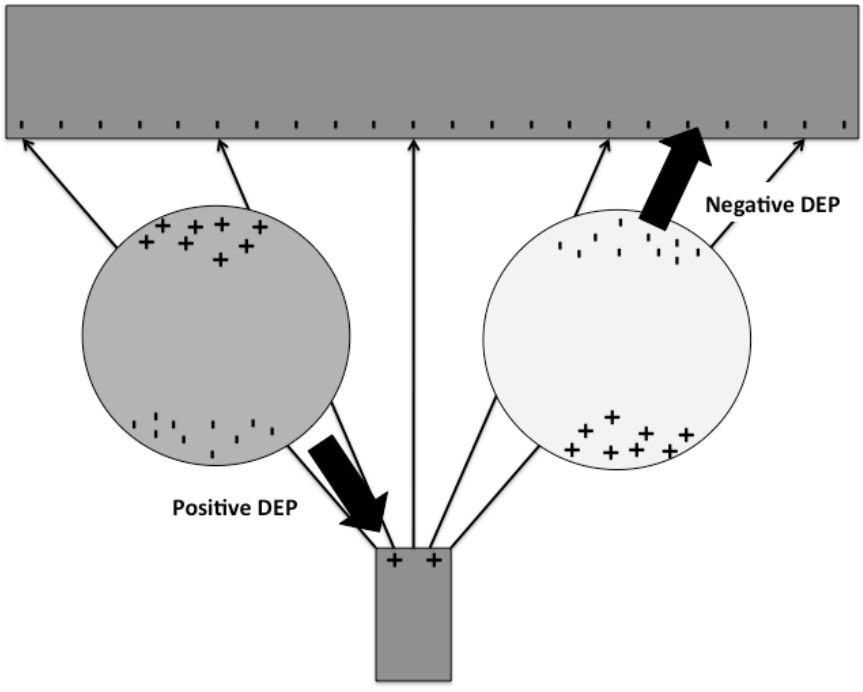

(b)

Figure 5: Positive and negative dielectrophoresis for more polarizable particle and less polarizable particle in uniform (a) and non-uniform electric field (b).

As can be observed from Figure 5(a), there is a net zero force in dielectrophoresis in a uniform electric field. This is due to the fact that there is no spatial gradient of the electric field in a uniform electric field. However, there is a net force towards the direction parallel or anti-parallel to the electric field when there is a non-uniform electric field as can be seen from Figure 5(b). If the dielectrophoretic force is parallel to the electric field, it is called positive dielectrophoresis and it is called negative dielectrophoresis if it is anti-parallel. As can be observed from the dielectrophoretic force, the Clausius-Mossoti factor plays a role in determining whether the dielectrophoretic force is negative or positive.

From Figure 6, negative dielectrophoresis occurs when the real part of the Clausius-Mossoti factor is negative and positive dielectrophoresis occurs when the real part of the Clausius-Mossoti factor is positive. [17]

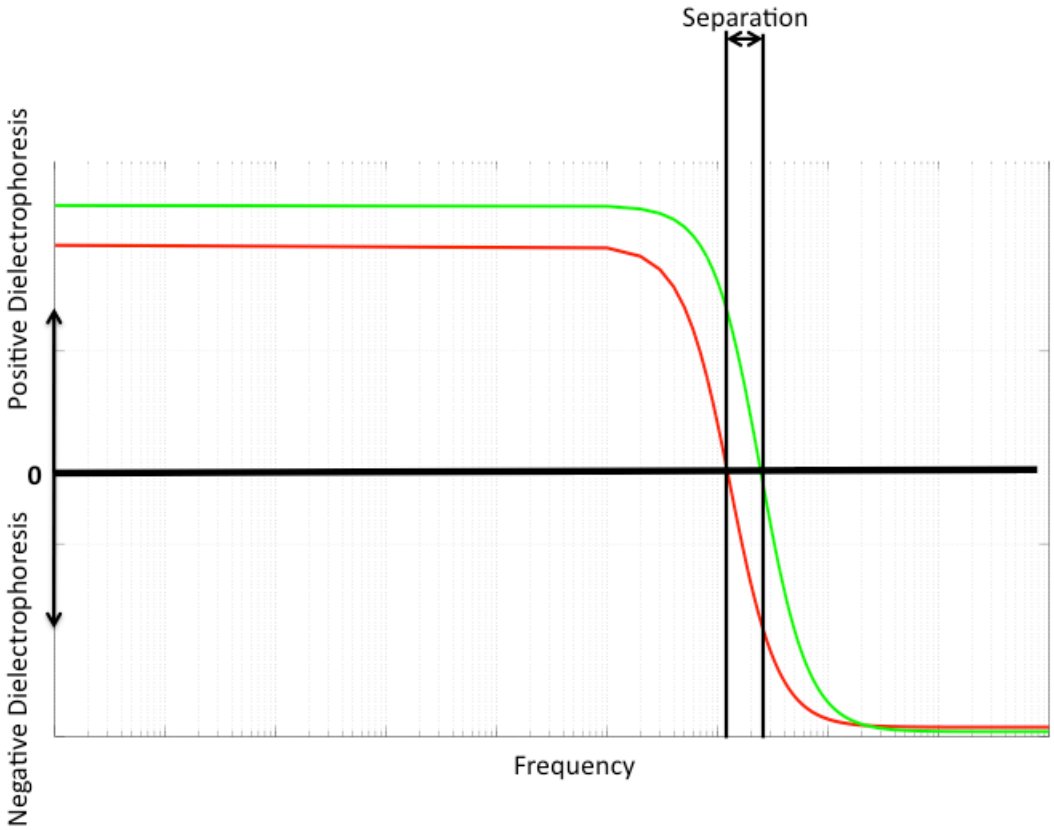

Figure 6: Plot of the Clausius-Mossotti factor for two different particles (solid and dotted lines) with respect to Frequency and the Separation of Particles using Dielectrophoresis.

Dielectrophoresis can be used to separate particles using positive and negative dielectrophoresis [17]. Taking figure 6 as an example, it can be seen that the two particles can be separated between the range where one (green) is undergoing positive dielectrophoresis while the other is undergoing negative dielectrophoresis (red) [17].

2.2.4 Particle Dipole-Dipole Attraction

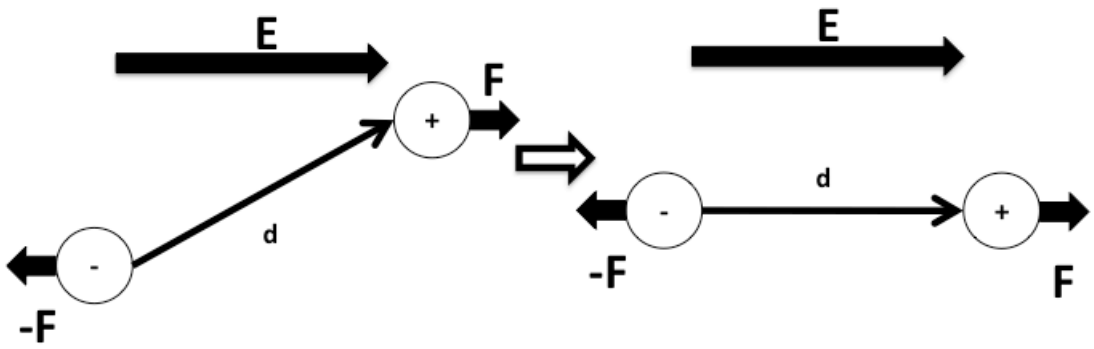

Figure 7: Dipole Moment.

Electric dipole is formed when two charges of same magnitude Q and opposite signs are distributed into two separate locations [17]. Consequently, this forms a vector from the negative charges to the positive charges called the dipole moment, *p* [17].

$$p = Qd \tag{7}$$

where *d* is the vector of the distance from negative to the positive charge.

Furthermore, the force on a dipole in an electric field is [17]

$$F = (p \bullet \nabla)E \tag{8}$$

Where *E* is the electric field.

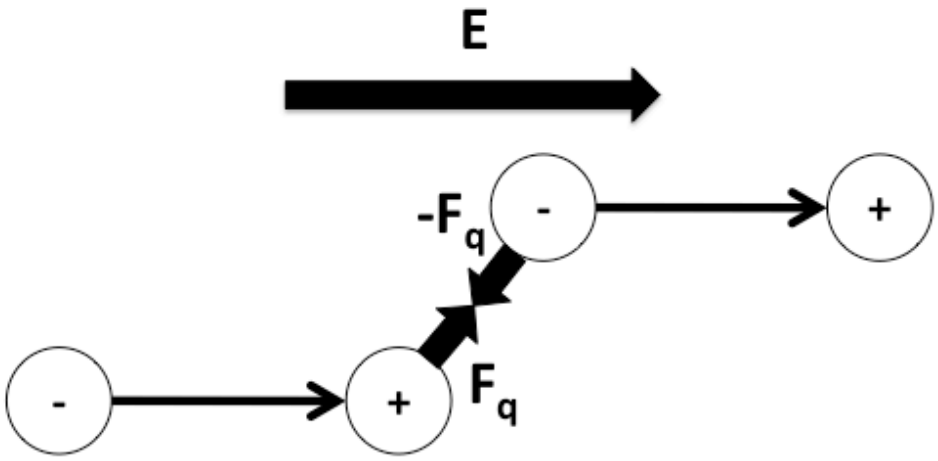

Figure 8: Attraction of two Fixed Dipoles.

A fixed dipole is when a molecule has a dipole moment in its natural state. As two fixed dipoles are close to each other, the positive end of the dipole is attracted to the negative end of the other dipole and this would cause the particles to form a chain [17]. Polarized particles also display a similar behavior as these dipoles.

On the other hand, an induced dipole is when a dipole moment is formed in a molecule or even a group of molecule with the introduction of an electric field. Objects like polystyrene particles can be inductively polarized under an electric field and this leads to an interesting phenomenon where particles are attracted or repulsed to each other which is observed in REP.

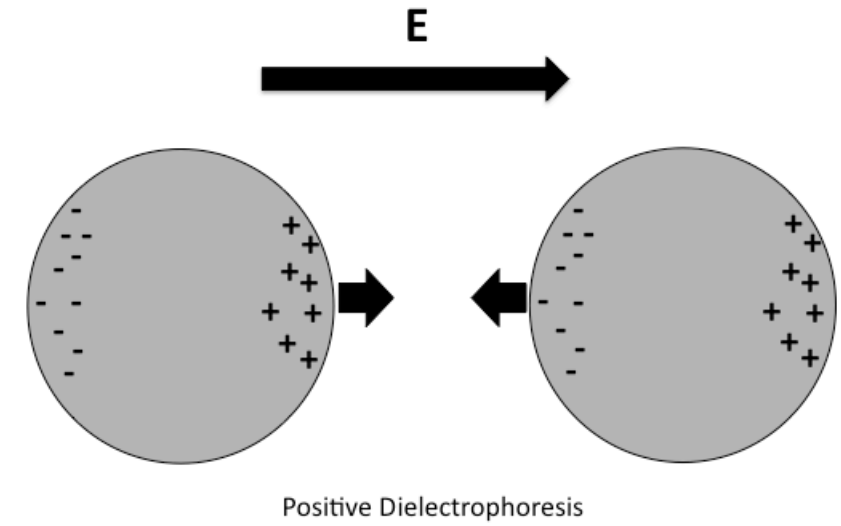

(a)

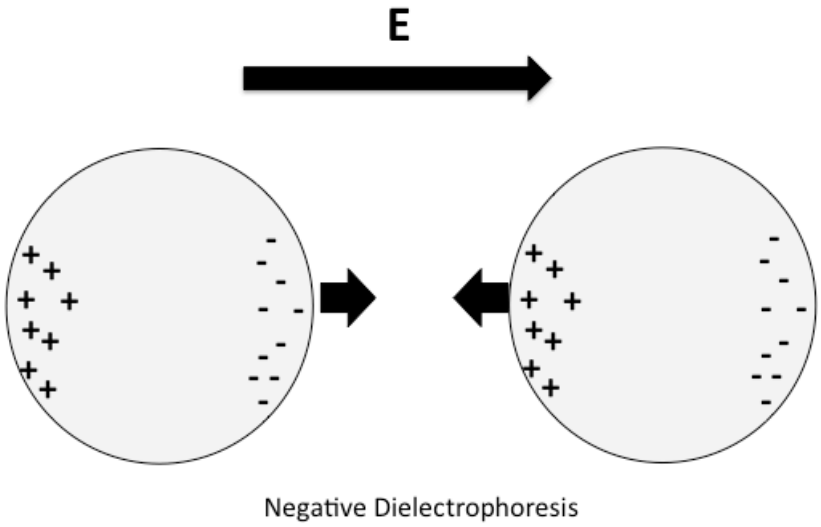

(b)

Figure 9: Particle-particle Interaction where two particles are aligned parallel to the electric field. (a) has particles that are more conductive than the solution and (b) has particles that are less conductive than the solution.

In Figure 9(a), both particles are more polarizable than the solution. The electric field strength inside the particles and at the edge of the particles perpendicular to the electric field are low while there are high electric field strength at the edge of the

particles that are parallel to the electric field especially between the two particles due to polarization. Both of these two particles experience positive dielectrophoresis and will move towards highest electric field strength and form a chain. In Figure 9(b), the particles are both less polarizable than the solution. The electric field strength inside the particles and at the edges of the particles perpendicular to the electric field are high while there are low electric field strength at the edge of the particles that are parallel to the electric field especially between the two particles due to polarization. Both of these two particles experience negative dielecterophoresis and will move towards lowest electric field strength and also form a chain. [17]

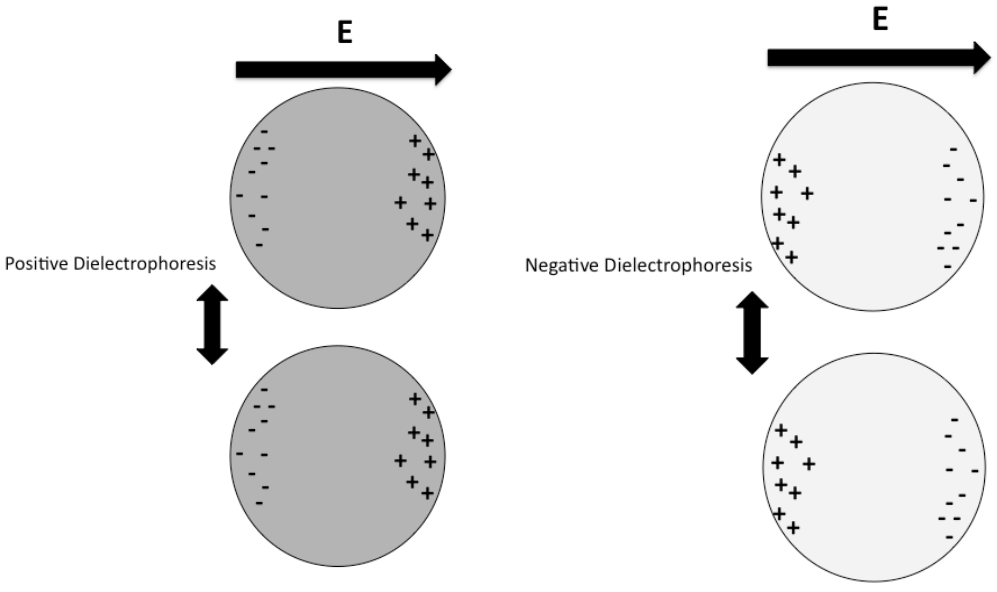

(a) (b)

Figure 10: Particle-particle Interaction where two particles that are aligned perpendicular to the electric field.

Next, the pair of particles is rotated 90° clockwise. In Figure 10(a), the particles experience positive dielectrophoresis and will repel each other as the surrounding

area of the particles not in between the two particles has a higher electric field strength compared to the area in between the two particles. The same occurs in Figure 10(b) where the particles experience negative dielectrophoresis and will repel each other as the surrounding area of the particles not in between the two particles has a lower electric field strength compared to the area in between the two particles. [17]

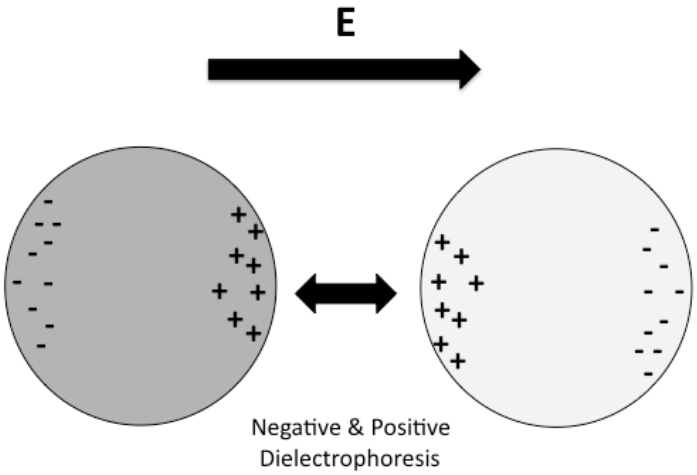

(a)

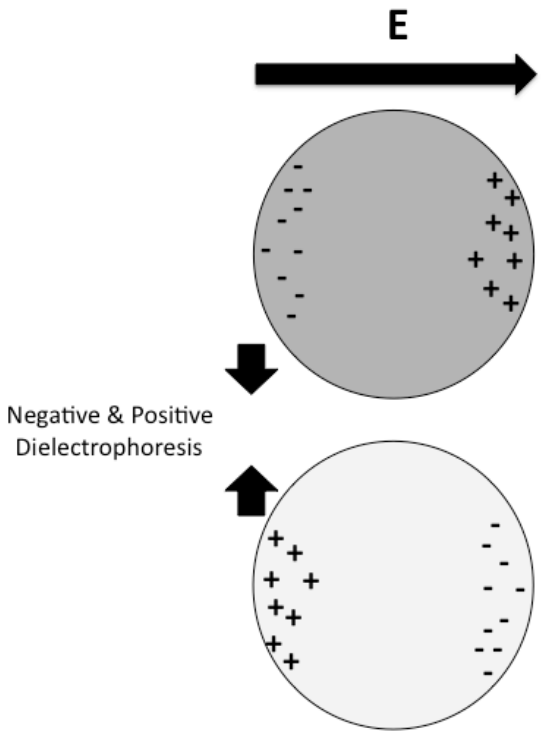

(b)

Figure 11: Particle-particle Interaction where two different particles are aligned parallel (a) and perpendicular (b) to the electric field.

These behaviors can also extend to particles of different polarizability. For Figure 11(a), the more polarizable particle (grey) and less polarizable particle (white) have distributions of the electrical strengths exactly like Figure 9. The less polarizable particle experiences positive dielectrophoresis and wants to move towards highest electric field strength while the more polarizable particle experiences negative dielectrophoresis and wants to move towards lowest electric field strength. As the highest and lowest electric field strength of the particle is parallel to the electric field but not between the two particles, the two particles will repel each other. On the other hand, Figure 11(b) has the distribution of electric field strength exactly like Figure 10. The less polarizable particle experiences positive dielectrophoresis and wants to move towards highest electric field strength while the more polarizable particle experiences negative dielectrophoresis and wants to move towards lowest electric field strength. As the highest and lowest electric field strength of the particle is perpendicular to the electric field and is in between the particles (more polarizable particle produce lowest electric field strength and less polarizable particle produce highest electric field strength), the two particles will attract each other. [17]

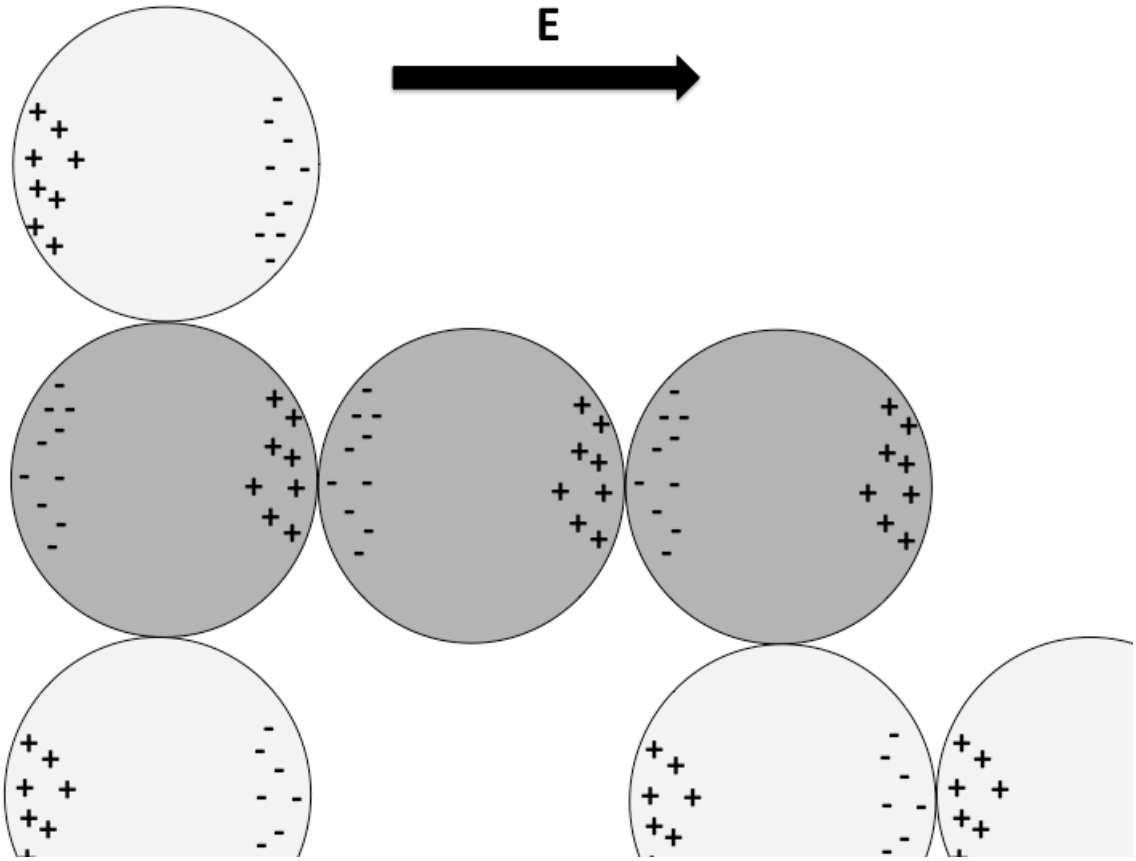

Figure 12: Chain forming of different particles in a solution applied with an electric field.

Thus, dielectrophoresis can be used to form chains of same particles or even a composite chain of different particles just like Figure 12.

2.2.5 Parameters for Particle Clustering

Studies have been conducted to study the relationship between different parameters that controls REP and cluster size [7].

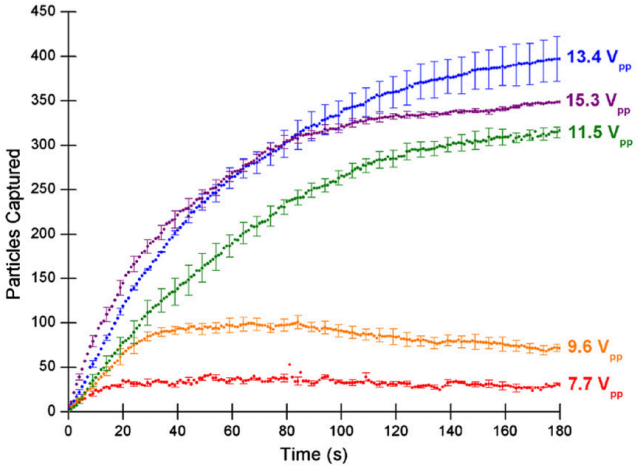

Figure 13: Accumulation of 1.0 um particles at the ITO electrode over a period of 3 min for various peak-to-peak voltages. Laser power is 23 mW and AC frequency is 70 kHz. (© IOP Publishing. Reproduced from Williams et al. by permission of IOP Publishing) [7].

As can be seen from Figure 13, it can be seen that, in general, the number of particles captured increases linearly and then plateaus as the particle cluster reaches steady state. Furthermore, it can also be observed that higher applied voltage causes larger number of particles captured except for 15.3 V_{pp}. This could be due to an increased electrothermal body force that is larger then the particle-particle and particle-electrode forces which would cause the particles to be forced out of the cluster.

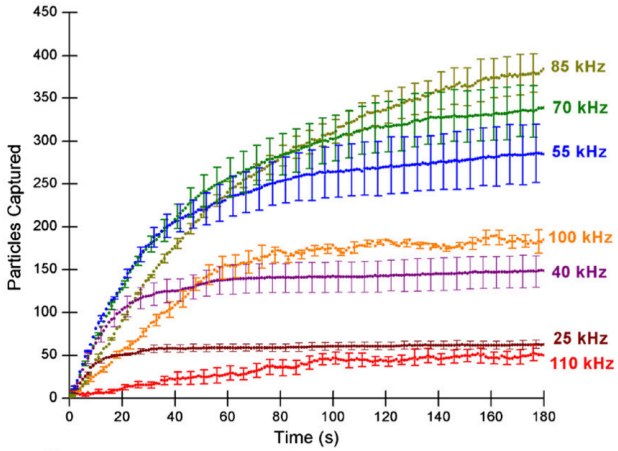

Figure 14: Accumulation of 1.0 um particles at the ITO electrode over a period of 3 min for various frequencies. Laser power is 23 mW and AC peak-to-peak voltage is 15.3 V_{pp}. (© IOP Publishing. Reproduced from Williams et al. by permission of IOP Publishing) [7].

From Figure 14, it can be observed that the particles captured for various frequencies starts out increasing linearly and then plateaus as the cluster reaches steady state. Furthermore, the particles captured increases, reaches a peak and then decreases as frequency increases. Thus, it seems that there is an optimum frequency that produces the largest particle cluster size.

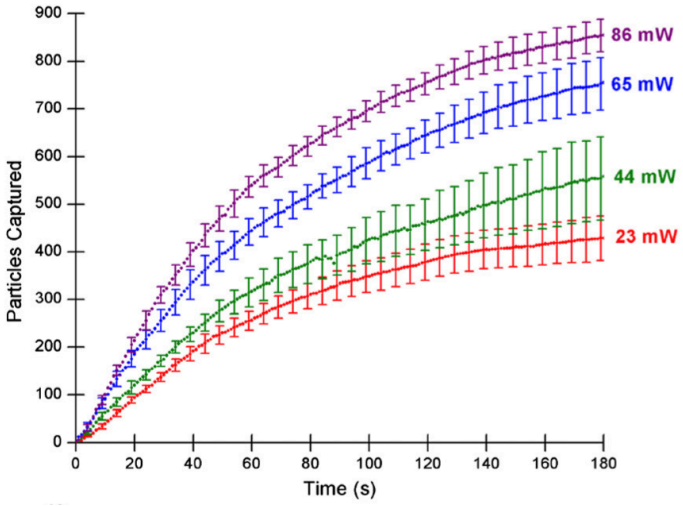

Figure 15: Accumulation of 1.0 um particles at the ITO electrode over a period of 3 min for various laser power. AC peak-to-peak voltage is 15.3 V_{pp}. and AC frequencty is 70 kHz. (© IOP Publishing. Reproduced from Williams et al. by permission of IOP Publishing) [7].

As with Figure 13 and Figure 14, Figure 15 shows that particle clusters increases linearly linear and then plateaus as the particle cluster reaches steady state. The increase in laser power increases the number of particles captured. This could be due to the electrothermal flow's velocity increases as laser power increases due to a steeper temperature gradient which leads to faster particle circulation and a higher probability to have a particle attracted to the cluster.

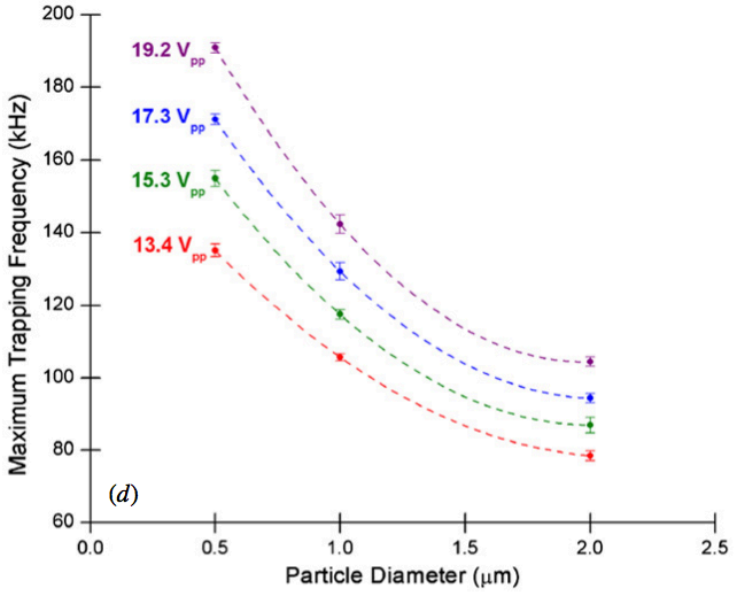

Figure 16: Maximum trapping frequency for particles of various diameters to cluster at different applied AC peak-to-peak voltage. Laser power is 23 mW. (© IOP Publishing. Reproduced from Williams et al. by permission of IOP Publishing) [7].

Figure 16 shows the maximum trapping frequency for particles of different diameters before it fails to form a cluster. A particle of smaller diameter will remain trapped at a higher frequency when compared to a larger particle. Furthermore, the maximum trapping frequency of the same particle increases as the applied AC peak-to-peak voltage increases.

2.3 Methodology

As stated before, fabrication of REP chips are relatively simple. The chip is made of a thin film electrode coated onto a glass substrate. The material that is typically used to conduct REP is ITO as it is transparent and would allow for observation inside the chip.

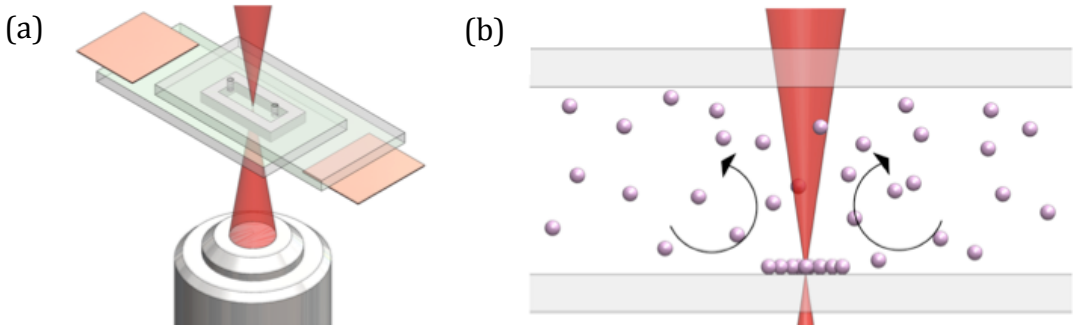

Figure 17: REP Chip.

With two of these substrates with electrodes facing each other, a spacer that was precut to define the microchannels is placed in between them to form the sidewalls. The spacer is any material that can be attached to both electrodes and is non-reactive to the electrodes and sample. In some cases, a commercial double-sided tape like Scotch® Removable Poster Tape, ¾" x 150" (3M Company, St. Paul, MN) can be used to conduct REP for short amount of time. The typical setup for conducting REP requires a laser source and an AC function generator. The laser will be applied to the desired location to conduct REP.

A technical requirement for the laser in REP is that the laser has to provide power that range between 0-20 mW. Furthermore, the laser frequency has to be considered so that the heat absorption of the laser onto the sample is minimal. AC power supply needs to provide 0-10 V with frequency of 30-200 kHz. It is advised that an oscilloscope is connected to the AC power supply to monitor the power output. [3-9]

Furthermore, lenses are typically chosen to be higher than 10X. This would ensure that the laser spot size is small to create a steeper temperature gradient [3-9].

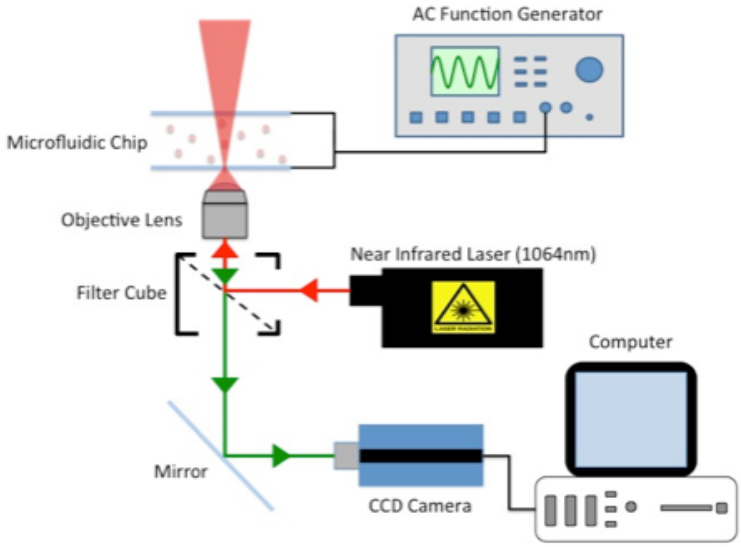

Figure 18: REP Setup.

The laser and camera is connected to an inverted Nikon TE2000U microscope. An AC function generator is connected to the elecrtrical contacts of the REP chip. As the laser travels into the microscope, the laser is reflected by a filter cube into the objective lens and is focused onto the chip's electrodes. The scattered light from the particles in the REP chip travels back into the objective lens, through the filter cube and into the camera, which is being controlled by a computer.

Particles are suspended in low conductivity solutions ($\sigma \leq 10$ mS/m). Electric double layer becomes thinner which increases the particle-electrode adhesion when particles are submerged in high conductivity solutions [3-9].

2.4 Current Applications

2.4.1 Differentiation of Biological Organisms

In 2012, Kwon et al. demonstrated that REP could trapping of bacteria Shewanella oneidensis and also collection of S. aureus from a S. aureus and S. cerevisae mixed solution. This shows potential application in the biological field [18].

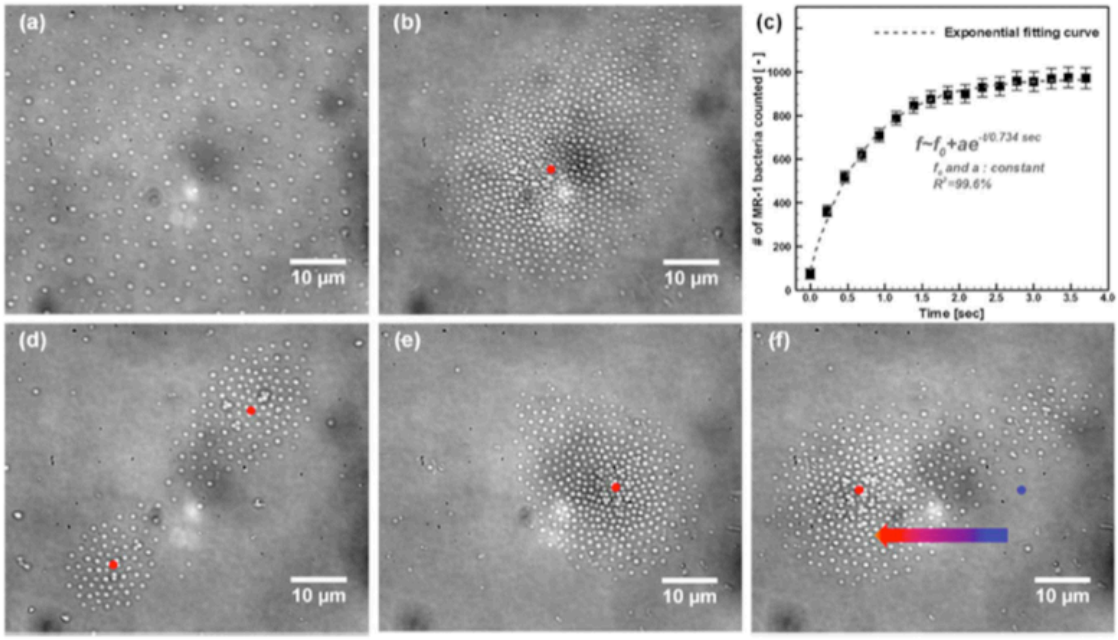

Figure 19: Trapping and Translation of S. oneidensis. (Reprinted with permission from Kwon et al. Copyright 2012 Royal Society of Chemistry)[18].

The major axis of Shewanella oneidensis, a 1 μm rod-shaped bacteria, was aligned with the electric field in the REP chip when the AC electric field was turned on. When the laser was turned on and focused on an electrode, the bacteria accumulates into a sizable cluster at the laser spot. It was also demonstrated that the cluster could be translated when the laser moved to another location. [18]

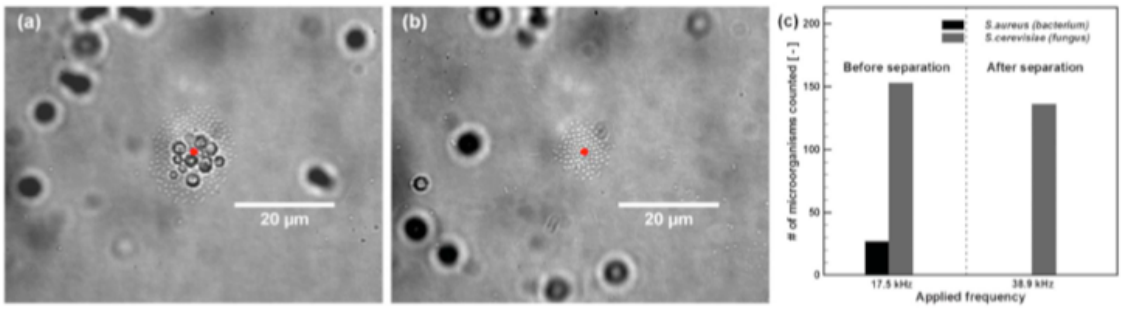

Figure 20: Separation of S. aureus from S. cerevisae. (Reprinted with permission from Kwon et al. Copyright 2012 Royal Society of Chemistry)[18].

Furthermore, Kwon et al. also demonstrated trapping and segregating organisms within an REP trap by changing the frequency of the AC electric field. Saccharomyces cerevisae, a 5 μm spherical shaped fungus, and Staphylococcus aureus , a ~1 μm spherical shaped bacteria, were both trapped under a 17.5 kHz frequency, 10.07 V_{pp} and 20 mW laser power . However, when the frequency increased to almost twice of the original frequency, the S. cerevisae were repelled away from the trap while the S. aureus remained in the trap. [18]

Overall, REP had no difficulty manipulating, trapping, and segregating biological organisms and this could open the doors potential applications in the biological field especially in cell culturing and bio-sensing.

2.4.2 Plasmonic Nanostructure to Optimize REP

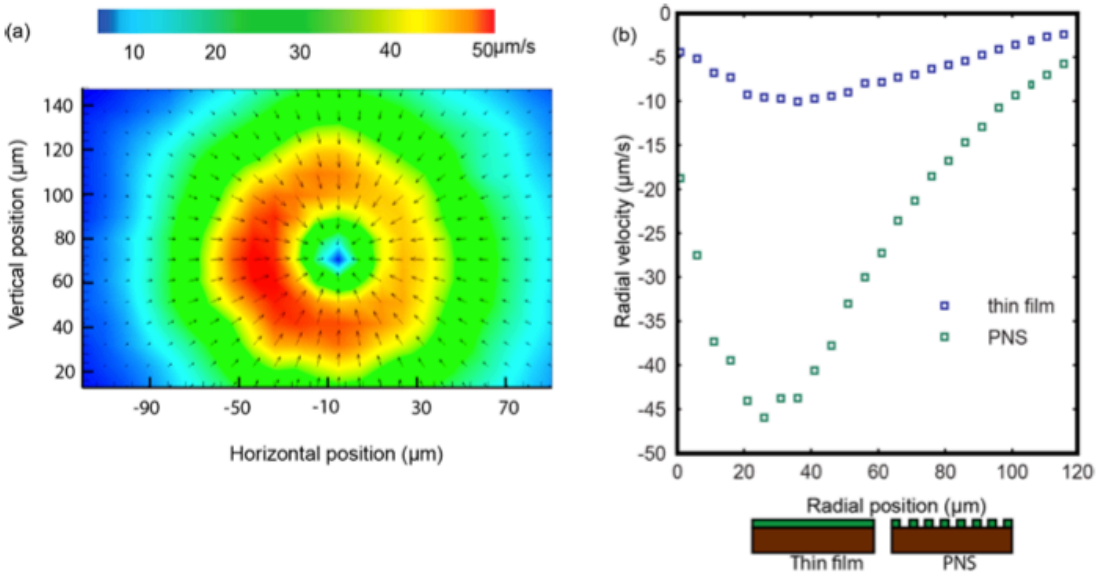

Figure 21: Plasmonice nanostructures: The velocity distribution (a) and radial velocity (b). (Reprinted with permission from Ndukaife et al. Copyright 2014 American Chemical Society)[19].

There have been many alternate designs for REP to reduce the cost of setting up a REP setup. One of the alternative designs for REP is to fabricate plasmonic nanostructures to increase the heating effects in a traditional REP chip . The nanostructures, array of gold nanodisks with diameters of 240 nm, that was fabricated was tuned to absorb light optimally at a specific wavelength. By exciting the structure at resonance frequency, a temperature gradient is produced and because the temperature gradient is significantly higher than a typical REP chip design, the electrothermal vortex also has a higher flow velocity. This higher flow velocity would in turn increase the chance of capturing particles into the REP trap. [19]

2.4.3 REP in Coplanar Electrodes

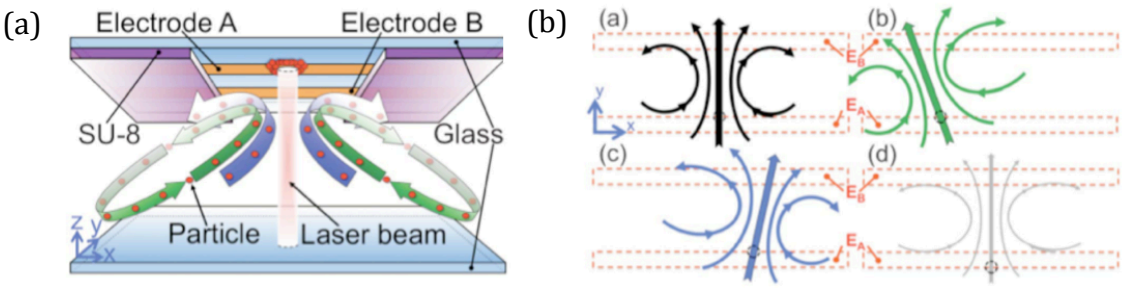

Figure 22: Twin Opposing Microvortices (TOMV). (Reprinted with permission from Park et al. Copyright 2012 Royal Society of Chemistry) [20].

Park et al. investigated twin opposing microvortices (TOMV). Two coplanar ITO electrodes were fabricated onto the glass surface with SU-8 partly covered. An AC electric field was applied while introducing a laser that is focused on the glass surface with the ITO electrode. The orientation of the TOMV can be changed within the chip when the laser is being focused at a different location which leads to a tunable microvortices device that can have different and interesting mixing effects when a laser is being focused at different locations. [20]

2.4.4 Thin Film Heaters as Heat Source for REP

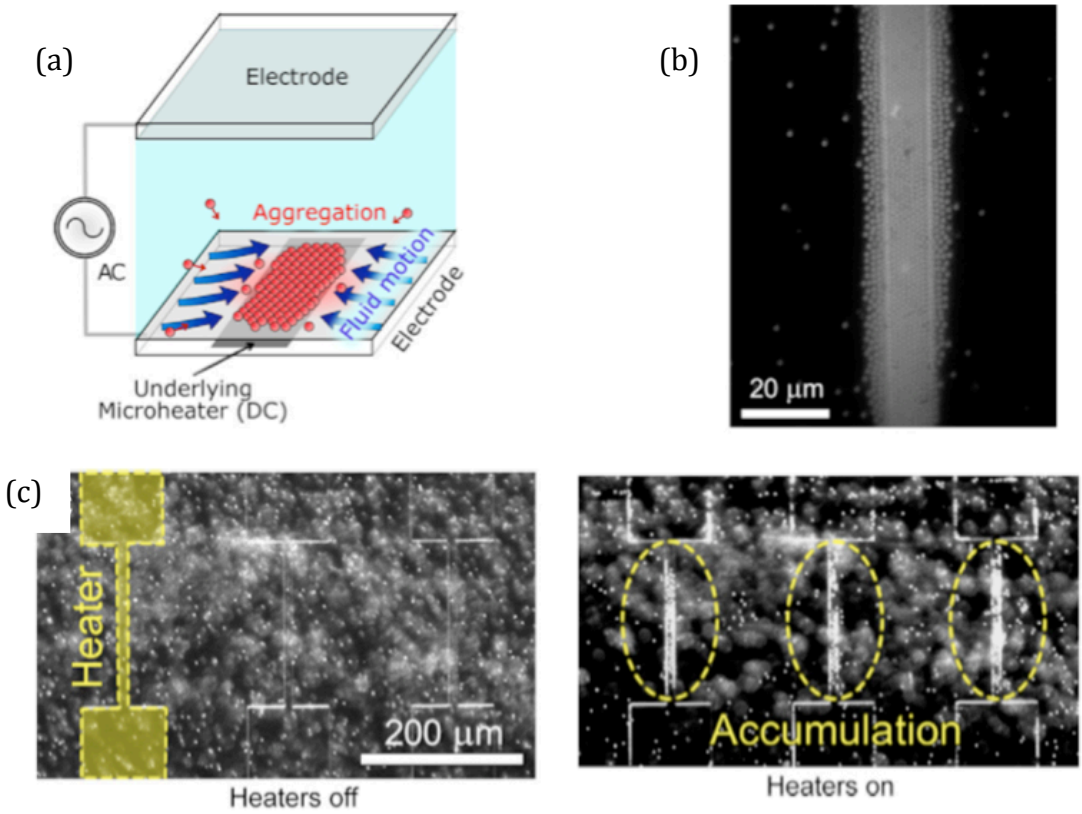

Figure 23: Conducting REP using thin film heaters as heat source. (Reprinted with permission from Velasco et al. Copyright 2012 Elsevier) [21, 22].

Williams et al and Velasco et al. looked into thin film heaters as an alternative for laser induced electrothermal flow. A 10 μm wide wire trace was used as the heating element which could produce 0.5 Kelvin temperature gradient. The system could trap, pattern, and sort particle cluster. This allows for a more affordable setup to conduct REP [21, 22]

2.5 Conclusions and Future Work

REP is desirable compared to other optoelectrokinetic techniques as it does not require any fabrication of electrode geometry, it is easy to fabricate and it is a non-contact technique that is consistent. Many applications are currently being looked into for REP and REP has the potential for many novel applications in the future.

CHAPTER 3: OPTIMIZING ELECTRODE THICKNESS AND MATERIAL FOR LASER-INDUCED ELECTROTHERMAL FLOW

3.1 Introduction

Rapid Electrokinetic Patterning (REP) is an optoelectric technique for non-invasive particle manipulation designed by Williams et al. [3-9]. By utilizing the electrothermal vortex, particle-particle interaction and particle-electrode interaction, REP is able to capture, translate and differentiate particles of different sizes.

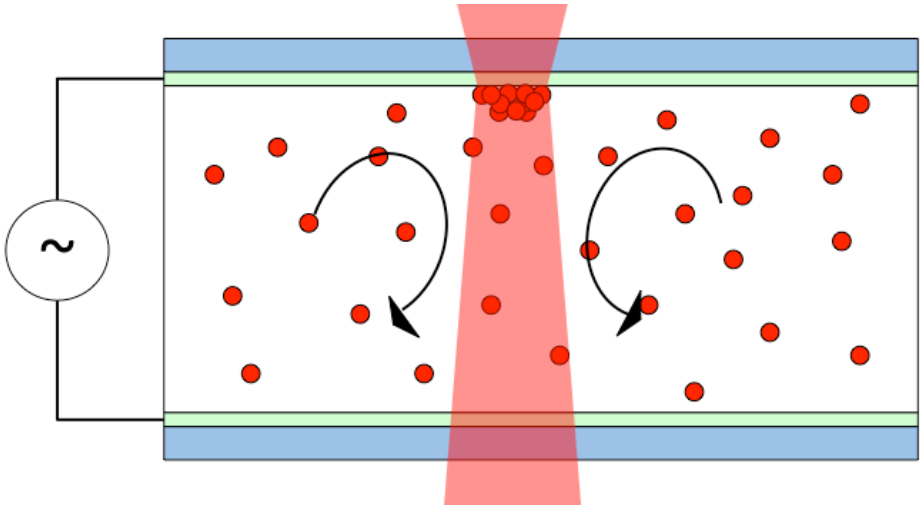

Figure 24: Illustration of REP with laser focused at the top electrode.

REP has many potential applications in fabrication and biosensing. It was demonstrated by Williams et al. that REP was able to manipulate and differentiate particles of different sizes and different materials [3-9]. Kwon et al. have used REP

to differentiate bacteria from fungus and also demonstrated the translation of the bacteria to another location [18]. There are many advantages to conducting REP compared with other techniques that require fabrication of electrode geometries. Firstly, REP is a non-contact technique where only a heating source and an AC electric field source are required to produce it. Secondly, REP does not require any prior electrode fabrication to manipulate particles. By translating the laser beam, particle clusters can be easily translated to another location. In the current setup, REP requires 4 $mW/\mu m^2$ to trap particles. The goal of this study is to investigate the possibility of reducing the laser intensity even further to minimize the damage to biological samples and lower the cost of the laser being utilized [10].

The electrode material is crucial for REP as electrodes are not only used to apply AC electric field but they also absorb the laser that is being focused onto the chip to produce temperature gradients that drive electrothermal vortex. In this study, the material dependence in thermal effects of electrothermal vortex will be accessed and analyzed to determine its role in REP. We have organized this paper in 3 key sections. First we present the theoretical model of laser induced heating of a thin layer on a glass substrate. This simple model provides us insight about the key parameters controlling the laser induced heating. It also shows that Ti and Ni can produce considerably higher temperature gradient than ITO. We then simulate electrothermal flow in COMSOL Multiphysics v4.4® to study laser induced heating and electrothermal flow in all its complexity. We mention the theory that governs

electrothermal flow followed by a brief explanation of the computational model. We then present experimental results of the velocity profile of the electrothermal flow for different materials. Experiments were performed to measure the electrothermal flow velocity profile using Micro-Particle Image Velocimetry (μPIV) for validating the computational model. Results reveal the same trend as in our analytical model where Ti and Ni appear to be far better material choices.

3.2 Theory

3.2.1 Reflection of the Laser at the Electrode Surface

The reflectance of the laser, *R* is the fraction of the light reflected to the incident light. By knowing the reflectance *R*, the light absorbed can be computed as it is just the remaining fraction of light that didn't get reflected away *1-R*.

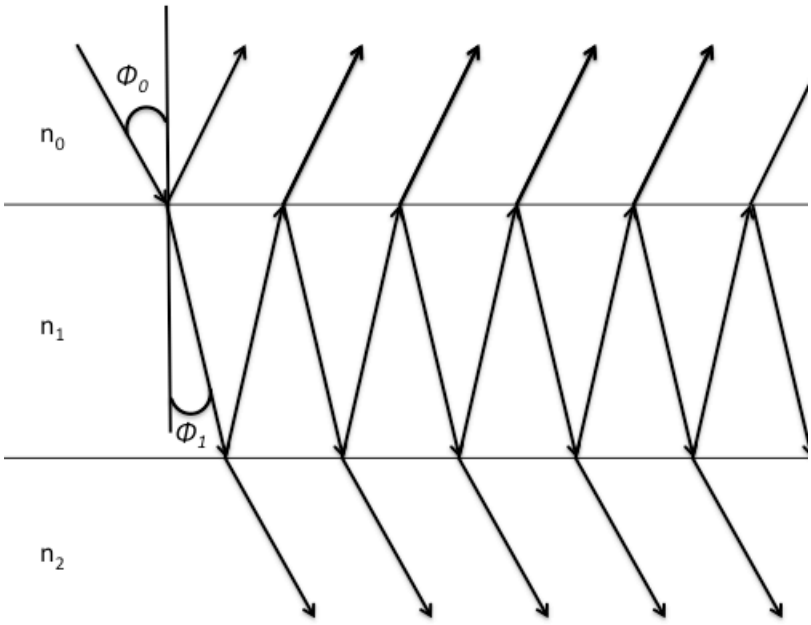

Figure 25: Propagation of Light (Reflection and Refraction) in Materials.

The reflectance can be calculated using Fresnel's equation.

$$R = \frac{r_1^2 + 2r_1 r_2 \cos 2\delta_1 + r_2^2}{1 + 2r_1 r_2 \cos 2\delta_1 + r_1^2 r_2^2} \tag{9}$$

where $r_1 = \frac{n_0 - n_1}{n_0 + n_1}$, $r_2 = \frac{n_1 - n_2}{n_1 + n_2}$, $\delta_1 = \frac{2\pi}{\lambda} n_1 d_1 \cos\phi_1$, n is the complex index of refraction $n = n_r + ik$, n_r is the index of refraction and k is the extinction coefficient, λ is the light's wavelength, d is the material thickness, and ϕ is the angle of the light on the plane. The subscript numbers corresponds to the materials in Figure 25.

3.2.2 Production of Temperature Gradient in Electrodes

The heat equation governs the heat exchange at the surface boundaries of the boundary volume and also the heat generated or dissipated within the boundary volume in the course of time.

$$k\nabla^2 T + G = \rho c_p \frac{\partial T}{\partial t} \tag{10}$$

where k is the thermal conductivity of the material, G is the power density or heat generation by the laser, ρ is the density of the material, c_p is the specific heat capacity and t is time.

The heat generation in the material by the laser is defined as

$$G = (1 - R) I_0 \alpha e^{-(\alpha z + \frac{2r^2}{w^2})} \tag{11}$$

where R is the reflectance, I_0 is the intensity at the center of the beam, α is the absorption coefficient of the electrode, z is the distance travelled by the laser in the

material, *w* is the beam waist of the laser and *r* is the radial distance from the center of the beam. The general heat equation is solved to determine the temperature gradient produced in the chip.

3.2.3 Analytical Solution of Laser Heating onto a Thin Substrate

Solving the general heat equation using Green's Function, the derived analytical solution of the cw laser heating onto the thin electrode in an REP chip [23-25] is

$$T(r,z) = \left(\frac{Pw\alpha_1^{\,2}(1-R)}{\pi k_1}\right)\int_0^{\infty} \frac{e^{-\frac{\lambda^2}{4}} J_0\left(\frac{\lambda r}{w}\right)}{2\left((\alpha_1 w)^2 - \lambda^2\right)}\left(A - \frac{\lambda e^{-\alpha_1 z}}{\alpha_1 w}\right) d\lambda \qquad (12)$$

where A is $\dfrac{\left(\dfrac{k_1 \cosh\left(\frac{\lambda(z_1 - z)}{w}\right)}{k_2} + \sinh\left(\frac{\lambda(z_1 - z)}{w}\right)\right) + \left(\dfrac{\lambda}{\alpha_1 w} - \dfrac{k_1}{k_2} - \dfrac{\left(1 - \frac{\lambda}{\alpha_2 w}\right)\left(\frac{k_1}{k_2}\right)^2\left((\alpha_1 w)^2 - \lambda^2\right)}{\left(\frac{\alpha_1}{\alpha_2}\right)^2\left((\alpha_2 w)^2 - \lambda^2\right)}\right) e^{-\alpha_1 z_1} \cosh\left(\frac{\lambda z}{w}\right)}{\cosh\left(\frac{\lambda z_1}{w}\right) + \dfrac{k_1 \sinh\left(\frac{\lambda z_1}{w}\right)}{k_2}}$,

P is the laser power, k_1 is the thermal conductivity of the electrode, k_2 is the thermal conductivity of the solution, z_1 is the thickness of the electrode, α_1 is the optical absorption coefficient of the electrode and α_2 is the optical absorption coefficient of the glass. From this equation, it can be observed that there are a few important parameters that determine the temperature profile of the electrode. These parameters are the thickness of the electrode, reflectance of the electrode, thermal conductivity of the electrode material and solution, the optical absorption coefficient of the electrode and solution and the beam waist of the laser.

3.2.4 AC Electric Field in Solution

Equation (13) is derived from the charge conservation equation [15, 16].

$$\nabla E = -\frac{1}{\sigma_s}\frac{\partial \sigma_s}{\partial T}\nabla T \bullet E \tag{13}$$

where E is the applied AC electric field, σ_s is the conductivity of the solution and T is the temperature of the solution. This equation describes the AC electric field produced in the microchannel when conducting REP.

3.2.5 Fluid Mechanics and Electrothermal Flow

The Navier-Stokes equation governs the fluid exchange at the boundary surfaces at the boundary volume in the course of time.

Electrothermal flow is the flow produced by having a combination of an AC electric field and a heat source that produces a temperature gradient. Electrothermal flow can be solved using the Navier-Stokes equation together with an electrothermal body force [11-17]:

$$\frac{\partial u}{\partial t} + (u \bullet \nabla)u = -\frac{1}{\rho}\nabla p + F + \left\langle f_{ET} \right\rangle + \frac{\mu}{\rho}\nabla^2 u \tag{14}$$

where u is the flow velocity, t is time, F is the gravitational body force, $\langle f_{ET} \rangle$ is the time-averaged electrothermal body force, μ is the kinematic viscosity.

The electrothermal body force is given by the following equation

$$\langle f_{ET} \rangle = \frac{\varepsilon_s}{2}[(\frac{1}{\varepsilon_s}\frac{\partial \varepsilon_s}{\partial T} - \frac{1}{\sigma_s}\frac{\partial \sigma_s}{\partial T})\frac{\nabla T \bullet E}{1+(\omega \frac{\varepsilon_s}{\sigma_s})^2}E - \frac{1}{2}\frac{1}{\varepsilon_s}\frac{\partial \varepsilon_s}{\partial T}|E|^2 \nabla T] \quad (15)$$

where ε_s is the permittivity of the solution, E is the applied AC electric field derived from Equation (15), ω is the angular frequency of the AC electric field. In the electrothermal body force, the first term of the equation is called the Coulomb force while the second term of the equation is called the dielectric force. Take note that the Coulomb force and the dielectric force subtract each other. In the current study, Coulomb force dominates the dielectric force.

3.3 Method and Materials

3.3.1 Chip Design and Fabrication

Experiments are conducted in a microchannel with a height of 280 μm. An electrically insulated double sided tape is trimmed to form microchannel in the microfluidic chip. This spacer was sandwiched between two electrodes that has suitable thermal and optical properties. A thin glass cover slip (Thermo Scientific, MA, USA) was attached to the side of the microchannel to be used as a window for viewing into the microchannel from the side, as shown in Figure 26. 700 nm and 70 nm (Indium Tin Oxide) ITO layers (SPI supplies Inc., PA, USA) were used as electrodes for the REP chip. Other than that, 60 nm and 80 nm Nickel layers (DRLI Inc., MO, USA) and 40 nm and 50 nm Titanium layer (DRLI Inc., MO, USA) were also used as electrodes for the REP chip.

Two holes were drilled into the top electrode to be the channel's input and output. After that, the electrodes and cover glass were solvent cleaned by ultrasonication in acetone, isopropanol for three minutes each. The electrodes and glass cover slip were later washed with distilled water and blow-dried with nitrogen gas. Lastly, copper tapes were adhered to the electrodes to act as electrical contacts. The bottom electrode was always the 70 nm ITO electrode as laser was always focused at the top electrode and it was preferable that the bottom electrode absorbs minimal radiation from the laser.

3.3.2 Experimental Setup

A Telulex Model SG-100/A signal generator (Berkeley Nucleonics Corp., CA, USA) was connected to the chip and the Agilent 54610B oscilloscope was used (Agilent Technologies, CA, USA) to observe the AC electrical signal. A 1064 nm continuous wave Nd:YVO_4 laser was equipped onto the inverted Nikon TE2000U microscope. Laser was focused at the top of the electrode with a Nikon 20x (0.45 NA) objective lens. Furthermore, a Nikon boom-stand microscope was installed to view the microfluidic chip from the side using a Nikon 10x (0.25 NA) objective lens. A camera (PCO.1600, Cooke Corporation, MI, USA) and a fluorescent illumination lamp (Xcite series 120PC, EXFO Life Sciences & Industrial Division, Ontario, Canada) were installed onto the boom microscope for image recording and illumination. For nickel and titanium REP chips, a Phantom v7.3 High Speed Camera (Vision Research Inc., NJ, USA) was used due to the higher flow velocity produced from the two electrodes.

PCO Camera was controlled using the manufacturer provided Camware® software. Phantom High Speed Camera was controlled by the manufacturer provided software, PCC version v2.6.749.0.

3.3.3 Particle Preparation

3.2 µm Fluoro-Max™ Red Fluorescent Polymer microsphere Particles (Thermo Scientific, MA, USA) were used as tracers for Particle Image Velocimetry (PIV) analysis. The particles are centrifuged from the native solution and dispensed in a KCl solution having 8.8 mS/m conductivity.

3.3.4 Software and Image Processing

Image processing to modify the contrast of the recorded image is conducted in MATLAB® (MathWorks® Inc., MA, USA) and Particle Image Velocimetry (PIV) evaluation is performed using DaVis 7.2 (LaVision Inc., MI, USA).

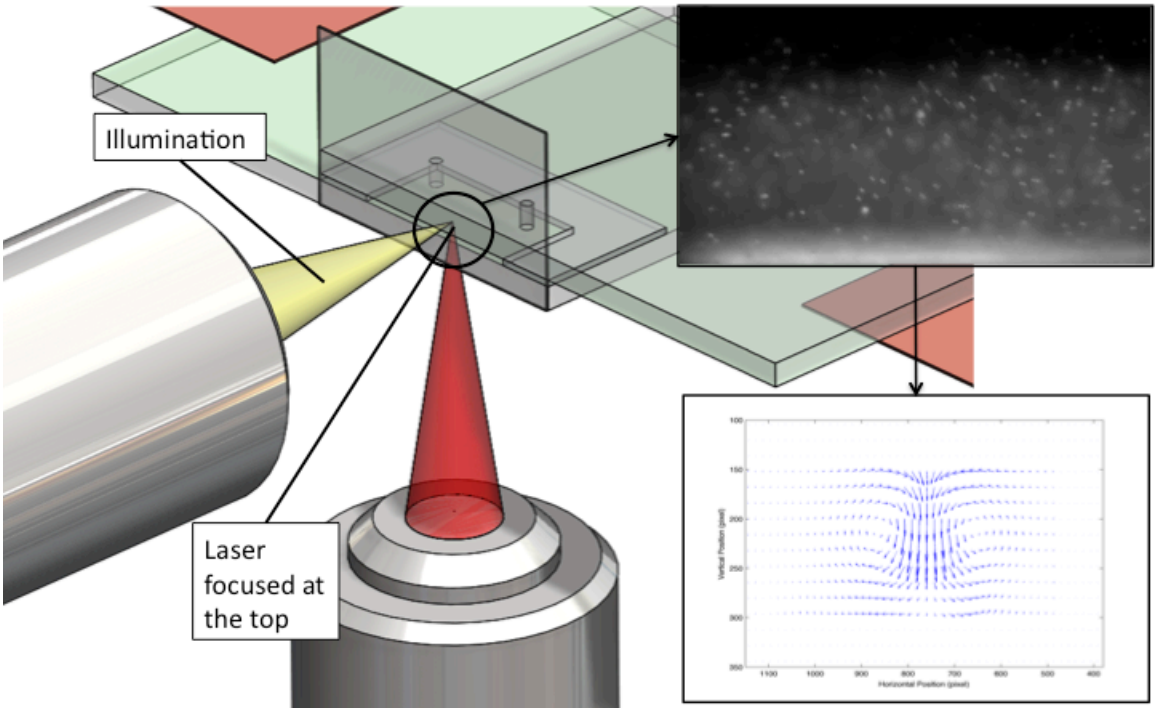

Figure 26: Experimental Setup and Method.

As can be seen in Figure 26, the laser, which is incident from the bottom of the chip, is focused at the top of the electrode while an objective lens connected to a boom-stand microscope is situated on the side to record the electrothermal flow. After that, PIV is conducted using Davis 7.2®. In all the experiments unless otherwise specified, an applied peak-to-peak voltage of 16 V and AC frequency of 100 kHz were used. Laser power was maintained at 41 mW.

3.4 Numerical Simulations

Simulations are conducted in COMSOL Multiphysics v4.4®. Apart from equations introduced in the theory section, there are some additional equations to be considered to simulate the electrothermal flow.

3.4.1 Production of Temperature Gradient in Electrodes

Temperature gradient in REP is produced by an external heating source, which in this case is a laser. The laser is modeled as a gaussian beam and included as a heat generation term in the steady-state heat equation [26].

$$k\nabla^2 T + G = 0 \tag{16}$$

where k is the thermal conductivity, G is the power density or heat generation by the laser.

The heat generation in the material by the laser is defined as

$$G = (1-R)I_0 \alpha e^{-(\alpha z + \frac{2r^2}{w^2})} \tag{17}$$

where R is the reflectance, I_0 is the intensity at the center of the beam, α is the absorption coefficient of the electrode, z is the distance travelled by the laser in the material, w is the beam waist of the laser and r is the radial distance from the center of the beam. The general heat equation is solved to determine the temperature gradient produced in the chip.

3.4.2 AC Electric Field in solution

Equation (18) is derived from the charge conservation equation [15, 16].

$$\nabla E = -\frac{1}{\sigma_s}\frac{\partial \sigma_s}{\partial T}\nabla T \bullet E \tag{18}$$

where E is the applied AC electric field, σ_s is the conductivity of the solution and T is the temperature of the solution. This equation describes the AC electric field produced in the microchannel when conducting REP.

3.4.3 Electrothermal Flow

Electrothermal flow is the flow produced by having a combination of an AC electric field and a heat source that produces a temperature gradient. Electrothermal flow can be solved using the Navier-Stokes equation together with an electrothermal body force [11-17]:

$$(u \bullet \nabla)u = -\frac{1}{\rho}\nabla p + F + \langle f_{ET} \rangle + \frac{\mu}{\rho}\nabla^2 u \tag{19}$$

where u is the flow velocity, t is time, F is the gravitational body force, $\langle f_{ET} \rangle$ is the time-averaged electrothermal body force, μ is the kinematic viscosity.

The electrothermal body force is given by the following equation

$$\langle f_{ET} \rangle = \frac{\varepsilon_s}{2}[(\frac{1}{\varepsilon_s}\frac{\partial \varepsilon_s}{\partial T} - \frac{1}{\sigma_s}\frac{\partial \sigma_s}{\partial T})\frac{\nabla T \bullet E}{1+(\omega\frac{\varepsilon_s}{\sigma_s})^2}E - \frac{1}{2}\frac{1}{\varepsilon_s}\frac{\partial \varepsilon_s}{\partial T}|E|^2 \nabla T] \tag{20}$$

where ε_s is the permittivity of the solution, E is the applied AC electric field derived from Equation (18), ω is the angular frequency of the AC electric field. In the electrothermal body force, the first term of the equation is called the Coulomb force

while the second term of the equation is called the dielectric force. Take note that the Coulomb force and the dielectric force subtract each other. In the current study, Coulomb force dominates the dielectric force.

3.4.4 Simulation

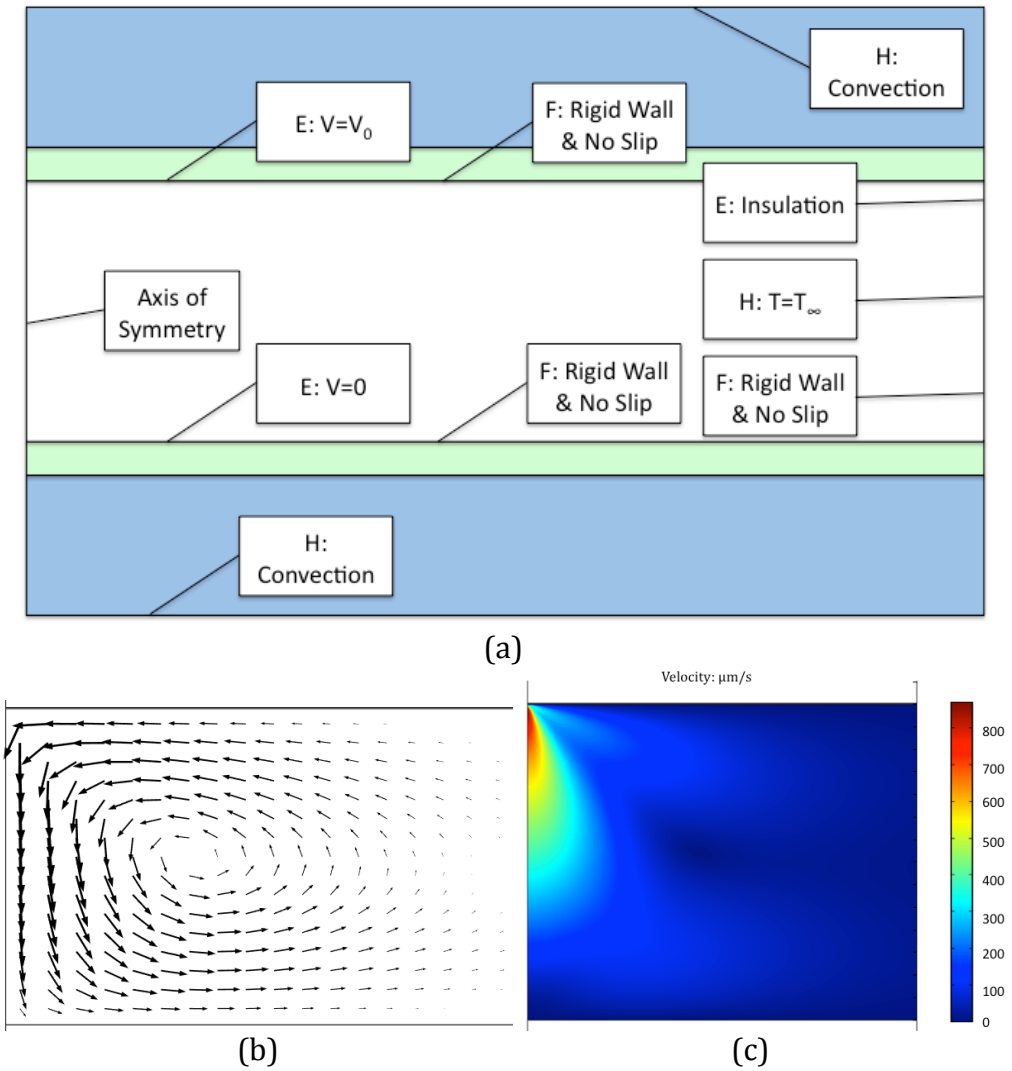

Figure 27: (a) Boundary conditions of the geometry in the simulation. E: AC Electric Field Model. H: Heat Transfer Model. F: Computational Fluid Dynamics Model. (b) Vector field of simulated electrothermal flow in logarithmic scale. (c) Contour plot of simulated electrothermal flow.

A 2-D axisymmetric model is used to conduct the simulation. The Non-Isothermal Flow package was utilized to simulate the temperature gradient and fluid flow. The coefficient form PDE module simulates the AC electric field produced in the fluid as the electric field is governed by the temperature gradient.

Table 1: Values of important properties for numerical simulation.

Symbol	**Property**	**Value**
P	Laser Power	41 mW
w	Beam Waist	2.4 μm
f	AC Frequency	100 kHz
alpha	Fractional Difference of Permittivity with respect to Temperature	-0.004 1/K
beta	Fractional Difference of Conductivity with respect to Temperature	0.02 1/K
er	Relativie permittivity	80 F/m
sigma	Conductivity	8.8 mS/m
hw	Channel Height	280 μm
w	Channel Length	10000 μm
hg	Thickness of Glass	700 μm
hITO	Thickness of Bottom Electrode	60 nm

In Table 1, the important properties for the numerical simulation are recorded. These properties will be use to compute and formulate the partial differential equations to be numerically simulated in the software.

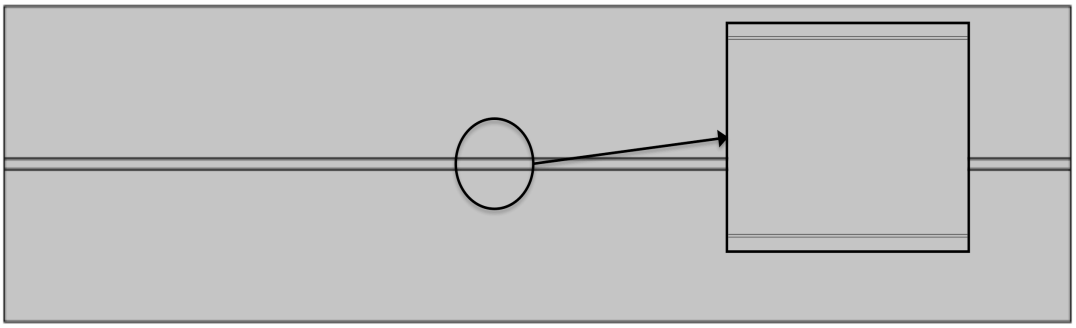

Figure 28: Final Geometry.

The geometry is constructed using five rectangles stack on each other to form a pair of glass substrates, a pair of electrodes and the microfluidic channel. These five rectangles are formed in union to each other to transform the geometries into the final geometry.

The heat generation of the laser is defined as an analytical function to be implemented in the heat equation in the simulation model. Materials are defined in the materials section using the materials library that is provided in the software.

Two simulation modules, Non-Isothermal Flow and Coefficient Form PDE, are utilized for the simulation of the electrothermal flow. The model is a 2D symmetrical model in cylindrical coordinates.

The Non-Isothermal Flow module is the pairing of the heat model together with the Computational Fluid Dynamics model. This is crucial for the simulation of the heated fluid from the electrodes. The electrodes absorb the laser and the heat absorbed

from the laser is dissipated into the liquid. This simulation together with the electric field simulation is used to simulate the electrothermal flow.

The electric field is modeled using the Coefficient Form PDE. COMSOL Multiphysics v4.4® does have a electrical module but because the electric field produced has a temperature dependence and it was decided that a custom PDE module should be constructed to model the electric field.

$$e_a \frac{\partial^2 F}{\partial t^2} + d_a \frac{\partial F}{\partial t} + \nabla \bullet \left(-c\nabla F - \alpha F + \gamma\right) + \beta \bullet \nabla F + aF = f \tag{21}$$

where the PDE is set up to match the electrical field equation in Equation (18).

Mesh geometry is a crucial component in computational modeling. The properties of the mesh geometry like element density, shape of the element, size of the element and etc. determines the stability of the computation and also the accuracy of the results of the computed numerical model. Thus, it is important to ensure that the mesh geometry is as optimum as possible. Ideally, the mesh geometry should be as fine as possible. However, the computational limit of the computer has to be considered as well when constructing the mesh geometry to ensure that the mesh construction and the computation in each individual element does not exceed the computational limit.

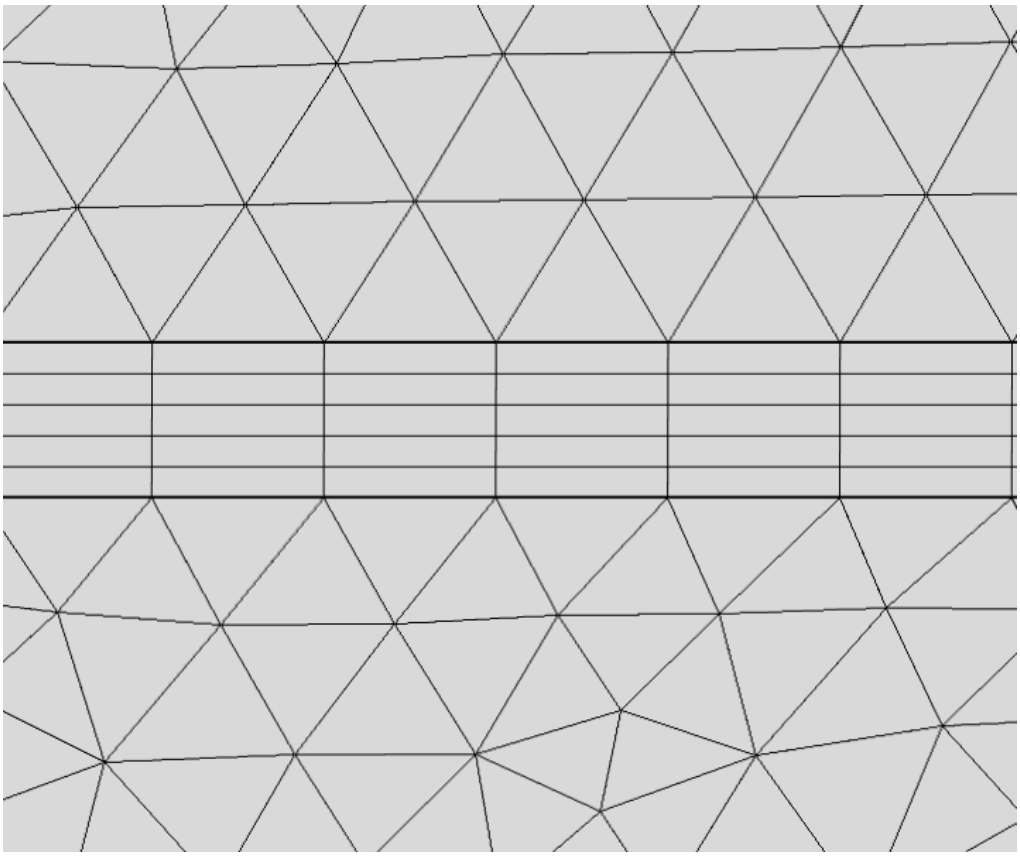

Figure 29: Free triangular meshing (top and bottom) and quadrilateral meshing (center).

The mesh constructed on the thin films is mapped with a quadrilateral mesh where locations of individual nodes are controlled to optimize mesh quality to take account for extremely high aspect ratio of the geometry as it is easy to customize. This is especially important to consider in this simulation as the simulation spans over a large range of length scales from electric field in channel (in μm range) to temperature gradient in electrode thickness (in nm range). This is the reason for the customization of the distribution of the element shape and size. Other parts of the meshes are constructed using free triangular meshing. The quality of mesh was ensured so that the computational results achieve mesh independence.

The simulation is solved in steady state using a three-step segregated stationary solver in which the temperature is solved initially, followed by the AC electric field and the obtained results from the first two segregated steps are used to solve for pressure and velocity in the last segregated step. These three steps are reiterated until the solution reaches a convergence with an absolute error of 10^{-6} as the maximum absolute error produced in the three segregated steps. A parametric sweep is also implemented to vary the electrode thickness in the desired range.

3.4.5 Comparison Between Experimental Results and Computational Results

When comparing the experimental results with the simulation results of the flow velocity of the electrothermal flow at the same location, it was found that they match with each other well. This proves that the computational model accurately depicts the physics of electrothermal flow in an REP chip and that the results produced from the computational model can be relied on. Take note that the objective lens used to focus the laser is 10x instead of 20x using the same laser power to prevent bubbles from forming at the focused spot.

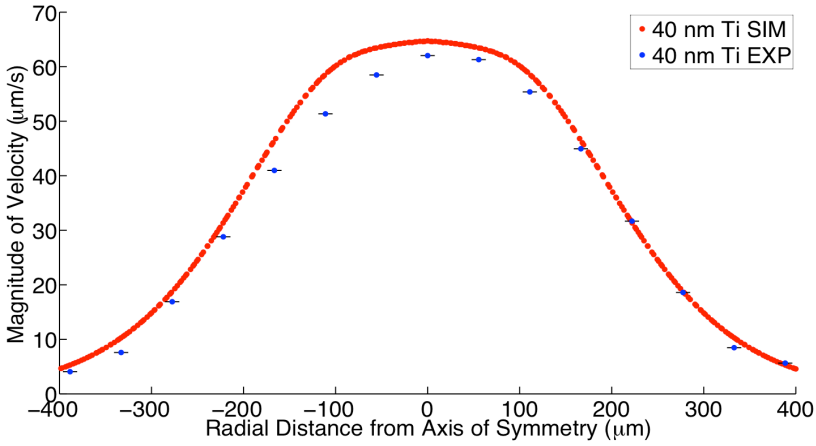

Figure 30: Comparison of velocity profiles of electrothermal flow of 40 nm Ti from experimental results and simulation at the same location.

3.5 Results and Discussions

Properties of the materials are needed for the analytical solution of the temperature produced in the laser heating and simulation of the electrothermal flow in REP. Table 2 is a table of all the essential properties of the material conducted in this study to simulate the electrothermal flow.

Table 2: Properties of various materials.

	ITO	**Ni**	**Ti**	**KCl**	**Glass**
Thermal Conductivity (W/m/K)	5.65	90.70	21.90	0.58	2.00
Density (kg/m^3)	7120	8900	4500	1000	2600
Heat Capacity (J/kg/K)	340.5	444.0	522.0	4200.0	840.0
Absorption Coefficient (m^{-1})	1.30E+05	5.59E+07	4.75E+07	60.6E-9	0
Optical Skin Depth (nm)	7692.31	17.90	21.06	-	-

3.5.1 Analytical Results of Temperature Difference per Laser Power

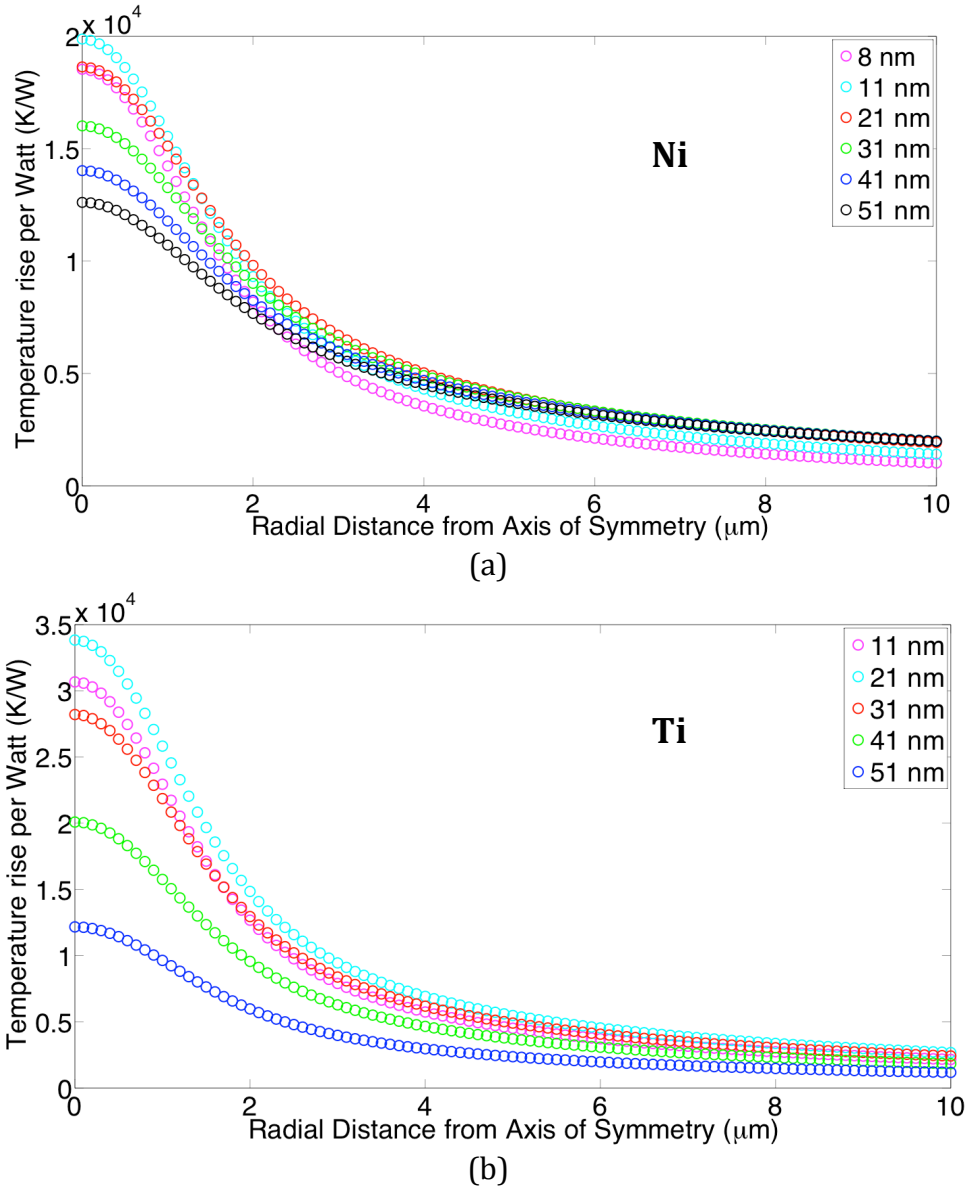

Figure 31: Temperature rise per laser power of Ni at (a) and Ti at (b) from analytical results.

From Figure 31, it can be observed that the temperature rise per laser power increases to an optimum peak and then decreases. These peaks occur approximately at the optical skin depth of the materials (Ni: 17 nm and Ti: 21 nm).

The possible explanation as to why this occurs is because when the material thickness is less than the optical skin depth is because the entire material layer absorbs the radiation from the laser. Furthermore, the thermal resistance of the material is high as the material is very thin which means heat does not easily conduct laterally. In this case, a thicker material layer will absorb more heat and consequently produce a higher temperature rise.

When the material thickness is more than the optical skin depth, the radiation is only absorbed within the material depth that is before the optical skin depth. Any distance after the optical skin depth is ideally not absorbing any radiation as the radiation has been absorbed entirely in the material layer that is less than the optical skin depth. This causes the trend of the temperature rise to be different. The temperature rise does not increase as the material thickness increase but rather it decreases as the material thickness increases. This is because the temperature gradient in the boundary at the optical skin depth is very high and heat would travel from a high temperature region to a low temperature region by Fourier's heat conduction law. Furthermore, the thermal resistance of the material is relatively lower than the thermal resistance of the thinner material as the thermal resistance is indirectly proportional to the material thickness. Thus, the low thermal resistance causes the lateral heat conduction to be relatively stronger than for thinner material. All of this causes the temperature rise of the material to decrease as the

material thickness increase for material thickness greater than the optical skin depth.

3.5.2 Analytical Solution and Computational Results of the Temperature Gradient

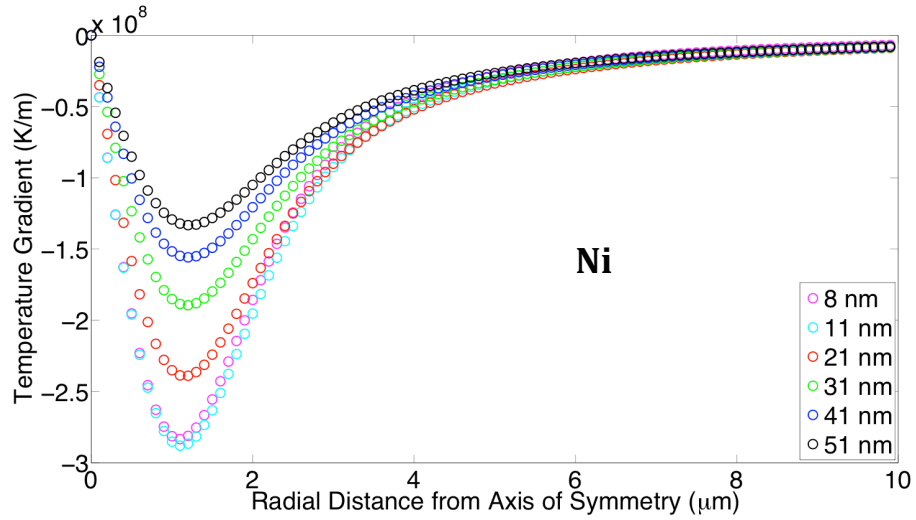

(a)

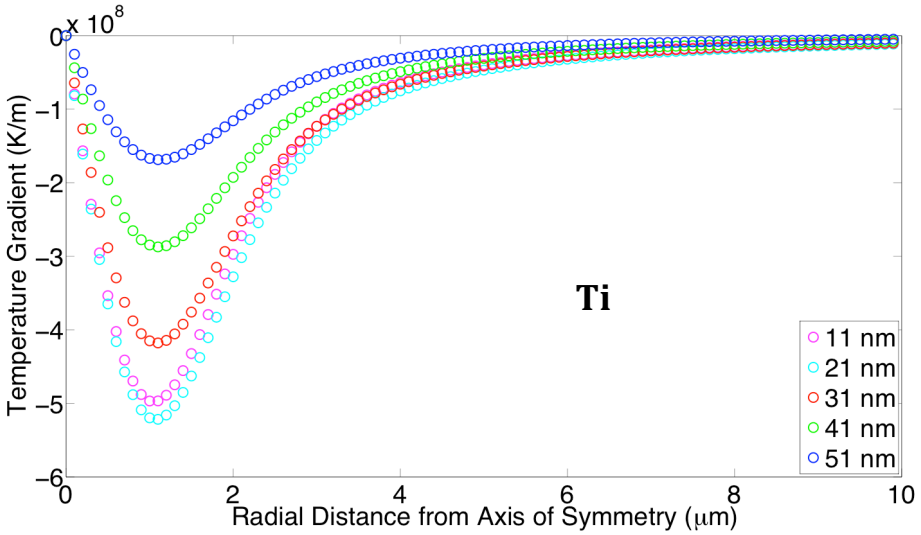

(b)

Figure 32: Temperature gradient of Ni at (a) and Ti at (b) from analytical results.

The temperature profile shown in Equation (18) was numerically integrated to compute the temperature gradient at the surface of the top electrode. It can be

observed that the temperature gradient increases as the thickness of the material increases until it reaches the maximum value that is around the optical skin depth of the material and then it decreases. This is due to the fact that when the material thickness is less than the optical skin depth, the increase in thickness would mean more volume to absorb the heat while when the material thickness is more than the optical skin depth, every part of the volume more than the optical skin depth does not absorb any heat as it has been absorbed entirely within the optical skin depth and this would leave more space for the heat to be conducted away from the absorbed spot, which makes the temperature gradient less steep.

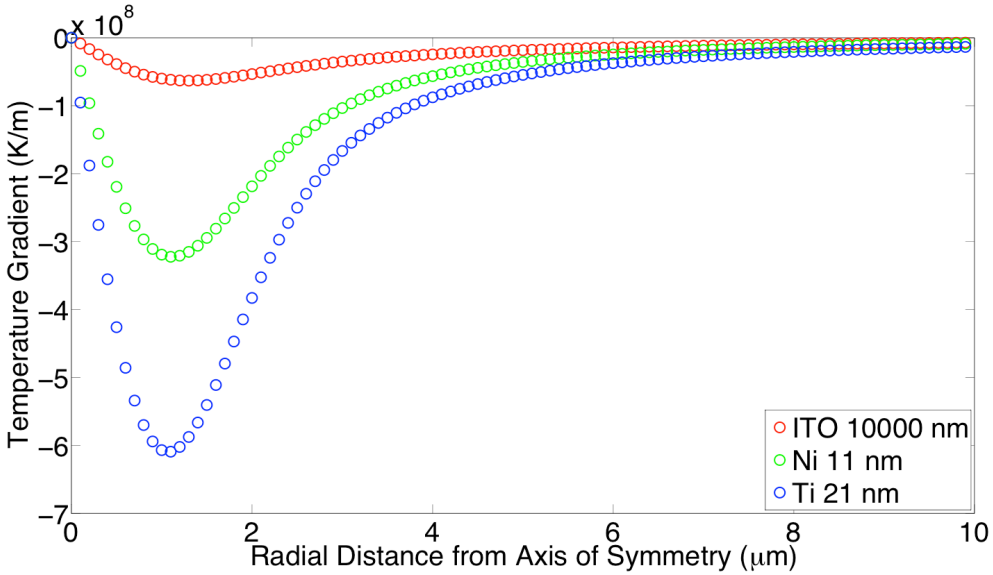

Figure 33: Steepest temperature gradient for ITO, Ni and Ti from analytical results.

Furthermore, titanium produced the steepest temperature gradient followed by nickel and then ITO when comparing the optimal thicknesses that produced the steepest temperature gradient for each material.

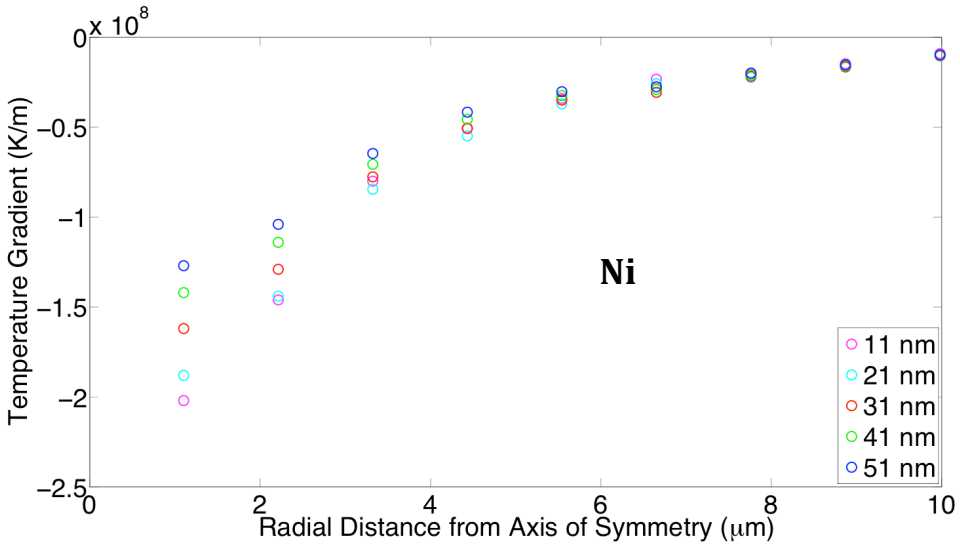

(a)

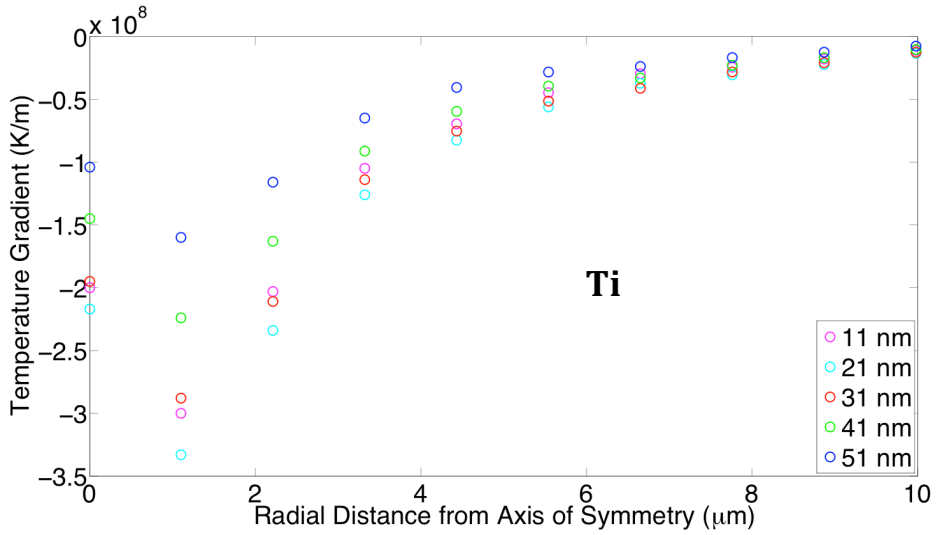

(b)

Figure 34: Temperature gradient of Ni at (a) and Ti at (b) from computational results.

From Figure 34, it can be seen that temperature gradient from computational results also follow this trend for Ti and Ni. When comparing the steepest temperature gradient in Figure 35 for the three materials, titanium also produced the steepest temperature gradient followed by nickel and then ITO.

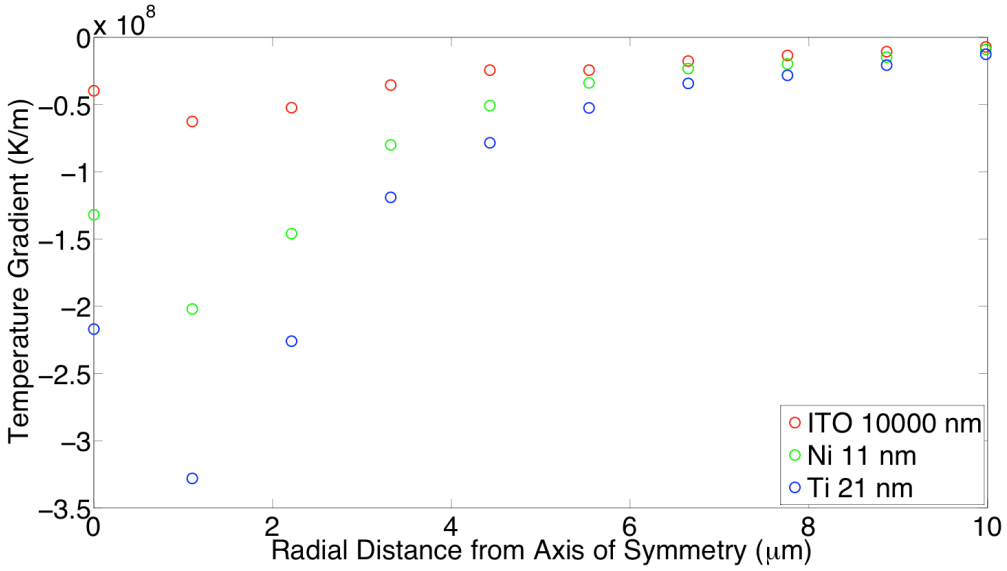

Figure 35: Steepest temperature gradient for ITO, Ni and Ti from computation results.

3.5.3 Comparison of Flow Velocity of Electrothermal Flow for Materials of Similar Thicknesses

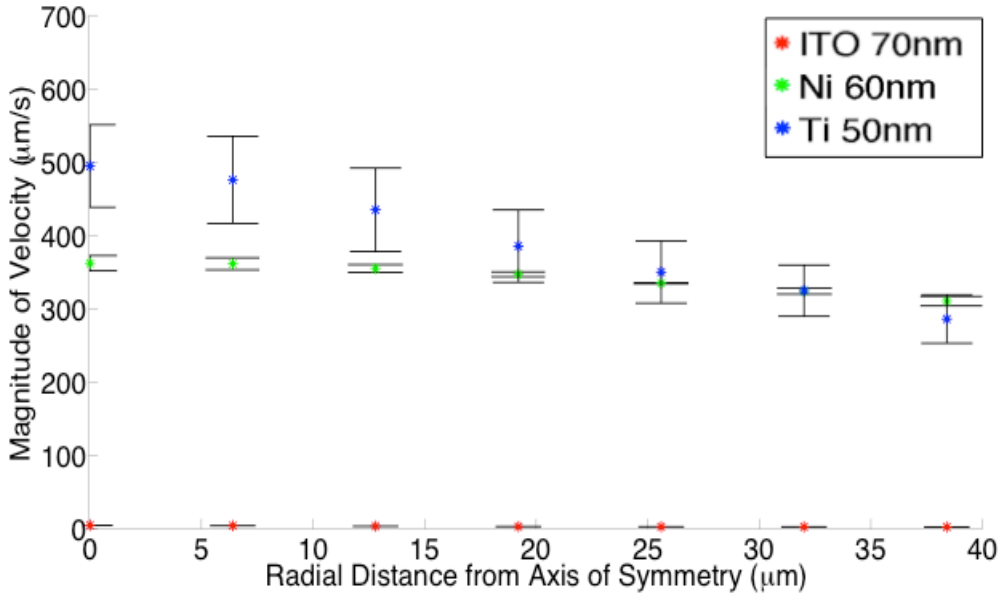

Figure 36: Experimental velocity profile of electrothermal flow by ITO, Ni and Ti of similar thicknesses at 30 V peak to peak and 201.8 μm above the bottom substrate in the channel.

Figure 36 shows the velocity profiles of the three materials (ITO, Ni, Ti) of similar thicknesses from experiments. The applied peak-to-peak voltage in this experiment is 30 V and vertical location relative to the bottom substrate in the channel is at 201.8 μm while all the other parameters stay the same. 30V is applied to ensure that 60 nm ITO electrode can produce a clearly observable velocity profile. Furthermore, for the titanium, the laser was focused at a location few micrometers below the top electrode as a bubble would form when focusing at the top electrode. With further comparison of the velocity profile, it can be observed that the electrothermal flow velocity produced from the titanium and nickel electrode is almost two orders of magnitude higher than 70 nm ITO. This also means that both Ni and Ti can produce the same flow velocity as 70 nm ITO with far lower laser power.

3.5.4 Optimal Material Thickness for Electrothermal Flow

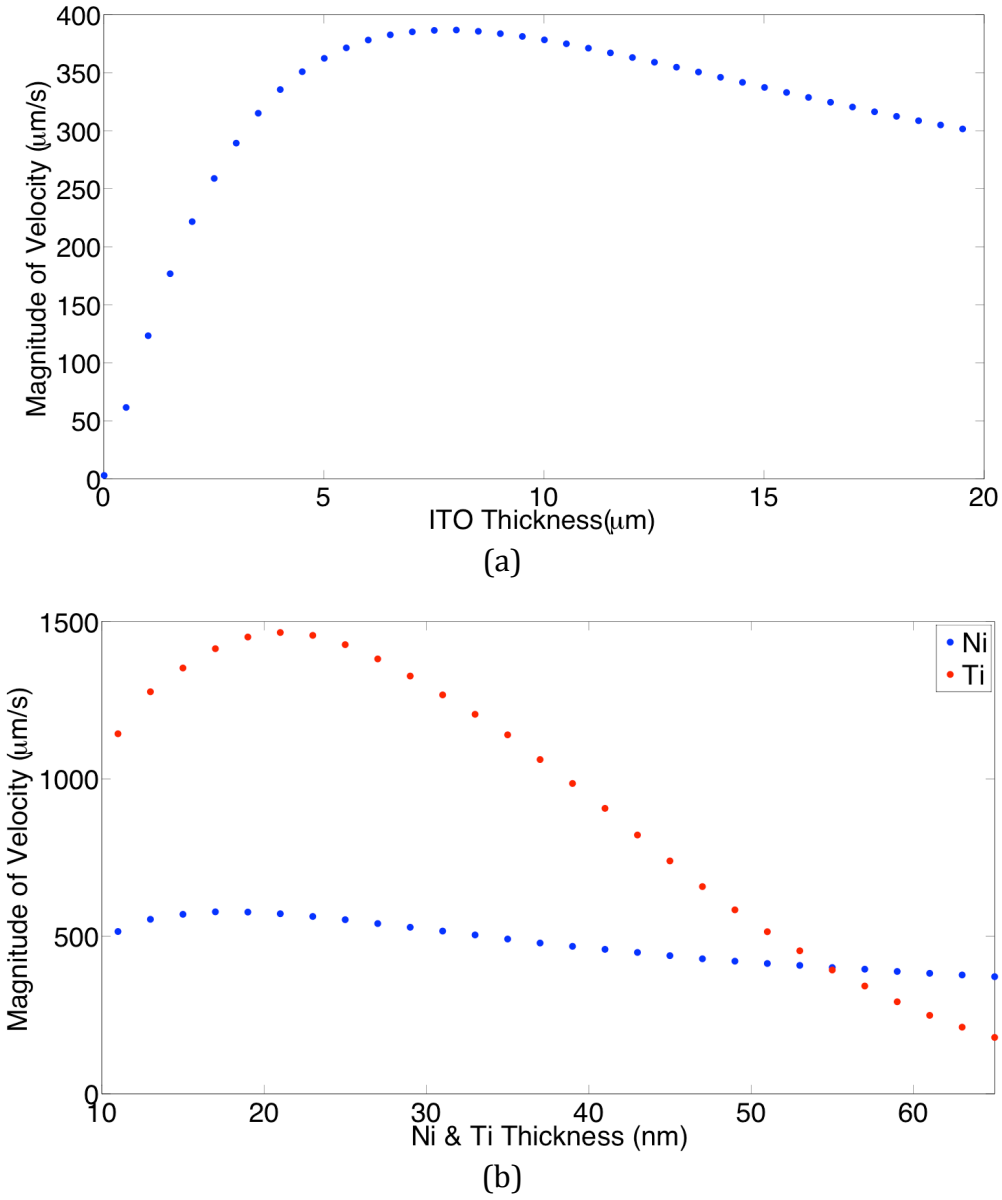

Figure 37: The relationship of the maximum velocity produced in the corresponding thickness for ITO at (a) and Ni and Ti at (b) at 30 V peak to peak and at 201.8 μm above the bottom substrate in the channel.

Furthermore, the simulation provides information on the optimal material thickness of each corresponding material to determine the electrothermal flow's maximum flow velocity. This will assists future adopters of REP to specifically determine the

desirable material thicknesses for their applications. The thickness of the material at its maximum velocity is 8011 nm for ITO, 17 nm for Ni and 21 nm for Ti.

3.6 Conclusion

In this study, we have studied the effects of electrode material properties on optically activated electrothermal flow. It was found that the analytical model and the numerical model followed the same trend and the numerical model also matches with the experimental model very well. Furthermore, it was found that the computational model could predict the optimal material thickness to create an optimized electrothermal flow for that material. Three materials (ITO, Ti, Ni) were tested and it was found that Ti-coated electrodes can produce high electrothermal flow per watt of laser power. For the same thickness of ITO, Ni and Ti, experiments showed that the flow produced by Nickel and Titanium was two orders of magnitude higher than the electrothermal flow produced by ITO. With this study, REP can be improved significantly. Laser power required to run conventional REP could be reduced to a point where a low-cost laser can easily provide which will consequently improve the accessibility of REP. Furthermore, this study shows that by simple selecting the proper electrode, user can produce a toroidal electrothermal vortex with velocity range from few 100 nm/s to 1000 um/s. Overall, this study has successfully documented the effects of material properties on electrothermal flow in REP. Future works that can be pursued to understand REP is the study of the particle-particle interaction and particle-electrode interaction in REP. Together with

the study of electrothermal flow, they will allow for better understanding of the physical phenomena that are involved in REP.

LIST OF REFERENCES

LIST OF REFERENCES

[1] Whitesides, G. (2006). The origins and the future of microfluidics. *Nature*, *442*(7101), 368–373. doi:10.1038/nature05058

[2] Sackmann, E., Fulton, A., & Beebe, D. (2014). The present and future role of microfluidics in biomedical research. *Nature*, *507*(7491), 181–189. doi:10.1038/nature13118

[3] Kumar, A., Williams, S., & Wereley, S. (2008). Experiments on opto-electrically generated microfluidic vortices. *Microfluidics and Nanofluidics*, *6*(5), 637–646. doi:10.1007/s10404-008-0339-8

[4] Williams, S., Kumar, A., & Wereley, S. (2008). Electrokinetic patterning of colloidal particles with optical landscapes. *Lab on a Chip*, *8*(11), 1879–1882. doi:10.1039/B810787D

[5] Kumar, A., Cierpka, C., Williams, S., Kähler, C., & Wereley, S. (2010). 3D3C velocimetry measurements of an electrothermal microvortex using wavefront deformation PTV and a single camera. *Microfluidics and Nanofluidics*, *10*(2), 355–365. doi:10.1007/s10404-010-0674-4

[6] Kumar, A., Kwon, J.-S., Williams, S., Green, N., Yip, N., & Wereley, S. (2010). Optically modulated electrokinetic manipulation and concentration of colloidal particles near an electrode surface. *Langmuir : the ACS journal of surfaces and colloids*,*26*(7), 5262–72. doi:10.1021/la904661y

[7] Williams, S., Kumar, A., Green, N., & Wereley, S. (2010). Optically induced electrokinetic concentration and sorting of colloids. *Journal of Micromechanics and Microengineering*, *20*(1), 015022. doi:10.1088/0960-1317/20/1/015022

[8] Kwon, J.-S., & Wereley, S. (2013). Towards New Methodologies for Manipulation of Colloidal Particles in a Miniaturized Fluidic Device: Optoelectrokinetic Manipulation Technique. *Journal of Fluids Engineering*, *135*(2), 021306. doi:10.1115/1

[9] Mishra, A., Kwon, J.-S., Thakur, R., & Wereley, S. (2014). Optoelectrical microfluidics as a promising tool in biology. *Trends in Biotechnology*, *32*(8), 414421. doi:10.1016/j.tibtech.2014.06.002

[10] Vogel, A., & Venugopalan, V. (2003). Mechanisms of Pulsed Laser Ablation of Biological Tissues. *Chemical Reviews*, *103*(2), 577–644. doi:10.1021/cr010379n

[11] Ramos, A., Morgan., H., & Green, N. G. (1998). Ac electrokinetics: a review of forces in microelectrode structures. *Journal of Physics D: Applied Physics, 31, 2338.* doi:10.1088/0022-3727/31/18/021

[12] Green, N. G., Ramos, A., & González, A. (2000). Electric field induced fluid flow on microelectrodes: the effect of illumination. *Journal of Physics D: Applied Physics, 33, L13.* doi:10.1088/0022-3727/33/2/102

[13] Green, N. G., Ramos, A., González, A., & Castellanos, A. (2001). Electrothermally induced fluid flow on microelectrodes. *Journal of Electrostatics, 52(2), 71-87.* Retrieved from http://www.sciencedirect.com/science/article/pii/S0304388601001322

[14] Gonzalez, A., Ramos, A., Morgan, H., Green, N., & Castellanos, A. (2006). Electrothermal flows generated by alternating and rotating electric fields in microsystems. *Journal of Fluid Mechanics*, *564*, 415. doi:10.1017/S0022112006001595

[15] Hawkins, B., & Kirby, B. (2010). Electrothermal flow effects in insulating (electrodeless) dielectrophoresis systems. *ELECTROPHORESIS*, *31*(22), 3622–3633. doi:10.1002/elps.201000429

[16] Loire, S., Kauffmann, P., Mezić, I., & Meinhart, C. (2012). A theoretical and experimental study of ac electrothermal flows. *Journal of Physics D: Applied Physics*,*45*(18), 185301. doi:10.1088/0022-3727/45/18/185301

[17] Morgan, H., & Green N. G. (2002) AC Electrokinetics: colloids and nanoparticles. Research Studies Pr; 1st Edition. Microtechnologies and Microsystems (Book 2) ISBN: 0863802559, 9780863802553

[18] Kwon, J.-S., Ravindranath, S., Kumar, A., Irudayaraj, J., & Wereley, S. (2012). Opto-electrokinetic manipulation for high-performance on-chip bioassays. *Lab on a Chip*,*12*(23), 4955–4959. doi:10.1039/C2LC40662D

[19] Ndukaife, J., Mishra, A., Guler, U., Nnanna, A., Wereley, S., & Boltasseva, A. (2014). Photothermal heating enabled by plasmonic nanostructures for electrokinetic manipulation and sorting of particles. *ACS nano*, *8*(9), 9035–43. doi:10.1021/nn502294w

[20] Park, C., & Wereley, S. (2013). Rapid generation and manipulation of microfluidic vortex flows induced by AC electrokinetics with optical illumination. *Lab on a Chip*,*13*(7), 1289–1294. doi:10.1039/C3LC41021H

[21] Williams, S. (2013). Enhanced electrothermal pumping with thin film resistive heaters.*ELECTROPHORESIS*, *34*(9-10), 1400–1408. doi:10.1002/elps.201200377

[22] Velasco, V., & Williams, S. (2013). Electrokinetic concentration, patterning, and sorting of colloids with thin film heaters. *Journal of Colloid and Interface Science*, *394*, 598603. doi:10.1016/j.jcis.2012.11.066

[23] Lax, M. (1977). Temperature rise induced by a laser beam. *Journal of Applied Physics*,*48*(9), 3919. doi:10.1063/1.324265

[24] Lax, M. (1978). Temperature rise induced by a laser beam II. The nonlinear case.*Applied Physics Letters*, *33*(8), 786. doi:10.1063/1.90505

[25] Calder, I. & Sue R. (1982). Modeling of cw laser annealing of multilayer structures. *Journal of Applied Physics*, *53*(11), 7545. doi:10.1063/1.330123

[26] Yilbas, B. S., Chapter 2 - Conduction-Limited Laser Pulsed Laser Heating: Fourier Heating Model, In Laser Heating Applications, Elsevier, Boston, 2012, Pages 7-51, ISBN 9780124157828, Retrieved from: http://dx.doi.org/10.1016/B978-0-12-415782-8.00002-4.

VITA

VITA

Jian Wei Khor

1513 Northwestern Avenue
West Lafayette, IN 47906
Cell: 765-237-2299
Email:jkhor@purdue.edu

Education

Purdue University-West Lafayette, IN, USA *Aug 2013 - Present*
M.S. in Mechanical Engineering **(**Expected Graduation: May 2015)
Advisor: Steven T. Wereley
GPA: 3.93 / 4.00

Purdue University-West Lafayette, IN, USA *Aug 2010 - May 2013*
B.S. in Mechanical Engineering
GPA: 3.70 / 4.00

Research Interest

- **Microfluidics**
- **Nanoscale Thermal Transport**
- Fabrication and Design of **Microelectromechanical Systems (MEMS) and Nanoelectromechanical Systems (NEMS)**

Research Experience

Birck Nanotechnology Center, West Lafayette, IN *Aug 2013 - Present*
Graduate Researcher
Material Dependence of Substrates in Electrothermal Flow for Optimization of an Electrokinetic Device

- Study of the effects of thermal and electrical properties of subtrates in electrothermal flows theoretically, experimentally and computationally
- Used COMSOL to conduct multiphysical simulations of the combination of laser heating and electric field generation to produce electrothermal flows

Flow Analysis of Aneurysm-on-a-Chip

- Conducted flow analysis on a microfluidic chip to compute wall shear stress
- Utilized Particle Image Velocimetry (PIV) to measure flow in the microfluidic channel

Birck Nanotechnology Center, West Lafayette, IN *May 2012 - May 2013*
Undergraduate Researcher
Simultaneous Measurement of Interfacial Surface Tension and Refractive index using Schlieren Imaging

- Designed a novel method of measuring surface tension and Refractive index simultaneously using Schlieren Imaging and Particle Image Velocimetry (PIV)

Professional Experience

Microfluidic Innovations LLC., West Lafayette, IN *Sept 2014 – Present*
Research Engineer

- Designed a novel device that levitates micrometer sized particles using acoustic levitation for pharmaceutical purposes (funding: a top five pharmaceutical company)

Publications

Book Chapters

1. K. Clayton, **J. W. Khor**, S. Wereley "Rapid Electrokinetic Patterning and its Applications," *Encyclopedia of Nanotechnology, 2nd Edition*. (Editor: Bharat Bushan). (Under Review)

Conference Proceedings and Presentations

1. **J. W. Khor**, A. Mishra, X. Pan, S. Wereley "Investigation of Material Dependence in Electrothermal Vortex," *67th Annual Meeting of the APS Division of Fluid Dynamics Volume 59, Number 20*, Nov. 23-25, 2014, San Francisco, CA (Presented by **J. W. Khor**)
2. A. Mishra, V. Kulkarni, **J. W. Khor**, S. Wereley "Low Interfacial Tension Measurement with Synthetic Schlieren Imaging," *66th Annual Meeting of the APS Division of Fluid Dynamics Volume 58*, Number 18, Nov. 24-26, 2013, Pittsburgh PA (Presented by A. Mishra)
3. A. Mishra, V. Kulkarni, **J. W. Khor**, S. Wereley "Surface Tension Induced Meniscus Measurement using Free Surface Synthetic Schlieren," *10th International Symposium on Particle Image Velocimetry*, Delft University of Technology, July 1-3, 2013, Delft, The Netherlands (Presented by S. Wereley)

Honors and Awards

- Dean's List & Semester Honors (6 in total) *Dec 2010 – May 2013*
- 2nd place in 2nd annual Stryker Engineering Challenge *Nov 2011*
- 5th place in Burton D. Morgan Business Plan Competition, Black Division (Undergraduate Division) *Feb 2013*

Extracurricular Activities and Volunteer Experience

- Graduation Composite Designer, School of Mechanical Engineering, Purdue University, *Jan 2012 – Dec 2012*
- Volunteer, Boiler Out Volunteer Program
  Nov 2012
- Volunteer, Carnival at Boys & Girls Club Lafayette
  Oct 2011

Membership

- American Physics Society (APS) *July 2014-Present*
- Pi Tau Sigma (Mechanical Engineering Honor Society) *Aug 2011-Present*

Skills, Languages and Qualifications

- **Laboratory Skills:** Microscopes, Boom Microscopes, Lasers, High Speed Cameras, Scientific Cameras, Oscilloscopes, Signal/ Function Generators, PIV Systems, Surface Tension measurement techniques and Power Amplifiers
- **Computer Skills:** MATLAB, COMSOL Multiphysics, LabView, CATIA, SolidWorks,
  MS Office, Particle Image Velocimetry (PIV), ImageJ
- **Basic Machining Skills:** Turning, Drilling, Milling, Shaping, Planing, Boring and Sawing
- Fluent in **Chinese Mandarin, English and Malay**
- **Engineer-in-Training (EIT)**; Successfully passed the Fundamentals of Engineering exam in the state of Indiana

Relevant Coursework

Purdue University, West Lafayette

- ECE557 – Integrated Circuit/ MEMS Fabrication Laboratory
- ME200 – Thermodynamics I
- ME300 – Thermodynamics II
- ME309 – Fluid Mechanics
- ME315 – Heat and Mass Transfer
- ME505 – Intermediate Heat Transfer
- ME508 – Heat Transfer in Biological Systems
- ME509 – Intermediate Fluid Mechanics
- ME517 – Micro/ Nanoscale Physical Processes
- ME587 – Engineering Optics
- ME592 – Fundamentals of Particle Image Velocimetry (PIV)